

Integrating high-throughput genetic interaction mapping and high-content screening to explore yeast spindle morphogenesis

Franco J. Vizeacoumar,^{1,2} Nydia van Dyk,^{1,2} Frederick S. Vizeacoumar,³ Vincent Cheung,⁵ Jingjing Li,^{1,2} Yaroslav Sydorsky,^{6,7} Nicolle Case,^{1,2} Zhijian Li,^{1,2} Alessandro Datti,³ Corey Nislow,^{1,2} Brian Raught,^{6,7} Zhaolei Zhang,^{1,2} Brendan Frey,⁵ Kerry Bloom,⁴ Charles Boone,^{1,2} and Brenda J. Andrews^{1,2}

¹Banting and Best Department of Medical Research and ²Terrence Donnelly Centre for Cellular and Biomolecular Research, University of Toronto, Toronto, Ontario M5S 3E1, Canada

³Samuel Lunenfeld Research Institute, Mount Sinai Hospital, Toronto, Ontario M5G 1X5, Canada

⁴Department of Biology, University of North Carolina, Chapel Hill, NC 27599

⁵Department of Electrical and Computer Engineering, University of Toronto, Toronto, Ontario M5S 3G4, Canada

⁶Ontario Cancer Institute, University Health Network, and ⁷Department of Medical Biophysics, University of Toronto, Ontario M5G 2M9, Canada

We describe the application of a novel screening approach that combines automated yeast genetics, synthetic genetic array (SGA) analysis, and a high-content screening (HCS) system to examine mitotic spindle morphogenesis. We measured numerous spindle and cellular morphological parameters in thousands of single mutants and corresponding sensitized double mutants lacking genes known to be involved in spindle function. We focused on a subset of genes that appear to define a highly conserved mitotic spindle disassembly pathway, which is known to involve Ipl1p, the

yeast aurora B kinase, as well as the cell cycle regulatory networks mitotic exit network (MEN) and fourteen early anaphase release (FEAR). We also dissected the function of the kinetochore protein Mcm21p, showing that sumoylation of Mcm21p regulates the enrichment of Ipl1p and other chromosomal passenger proteins to the spindle midzone to mediate spindle disassembly. Although we focused on spindle disassembly in a proof-of-principle study, our integrated HCS-SGA method can be applied to virtually any pathway, making it a powerful means for identifying specific cellular functions.

Introduction

A major challenge in post-genome biology is to exploit genome sequence information to produce reagents and technologies that decipher the molecular basis of gene function through an unbiased and systematic analysis. Although functional genomic approaches have been applied productively with yeast, the integration of multiple datasets is typically required to accurately define gene function. Combining data from many large-scale studies remains problematic because individual screens may not be saturating or conducted under comparable experimental conditions. To facilitate integration of large-scale phenotypic and genetic datasets, we combined an automated form of yeast genetics, synthetic genetic array (SGA) analysis (Tong et al.,

2001), with a high-content screening (HCS) system, which automates image acquisition and the quantification of specific morphological phenotypes.

We examined the morphological phenotypes of the growing mitotic spindle in both single gene deletion mutants and in selected double mutant arrays, sensitized for spindle defects. In addition, we also examined a subset of strains carrying conditional alleles of essential genes at both restrictive and permissive temperatures. For the implementation of the platform, each step, from sample processing to image acquisition and scoring of phenotypes, was automated and adapted for both live-cell and fixed-cell analysis. The cell biological phenotype of each yeast mutant

Correspondence to Brenda J. Andrews: brenda.andrews@utoronto.ca; and Charles Boone: charlie.boone@utoronto.ca

Abbreviations used in this paper: CPC, chromosomal passenger complex; FEAR, fourteen early anaphase release; HCS, high-content screening; MEN, mitotic exit network; SGA, synthetic genetic array; TAP, tandem affinity purification.

© 2010 Vizeacoumar et al. This article is distributed under the terms of an Attribution-Noncommercial-Share Alike-No Mirror Sites license for the first six months after the publication date [see <http://www.jcb.org/misc/terms.shtml>]. After six months it is available under a Creative Commons License [Attribution-Noncommercial-Share Alike 3.0 Unported license, as described at <http://creativecommons.org/licenses/by-nc-sa/3.0/>].

was represented by a quantitative readout of cellular parameters, called a morphological profile. Using this information, we identified 182 mutants that influence spindle dynamics, 90 of which had defects apparent only in the double mutant backgrounds. Our results identify new genes involved in spindle disassembly and outline an intricate pathway involving the SUMO machinery required for efficient relocalization of the Ipl1p kinase to the spindle midzone. Our SGA-HCS approach offers a general and powerful method for quantifying the activity of specific pathways in the context of complex genetic backgrounds.

Results

Systematic identification of mutants with aberrant spindle morphology

SGA methodology enables marked genetic elements to be combined in a single haploid cell through standard yeast mating and meiotic recombination via an automated procedure (Boone et al., 2007). Here, our goal was to systematically survey the yeast deletion collection for defects in spindle morphogenesis. To do so, we applied SGA to introduce a GFP-tubulin (GFP-Tub1p) reporter into the arrayed collection of deletion mutants. To sharpen our focus on spindle function, we also constructed double mutant arrays harboring GFP-Tub1p as well as a deletion allele of *BNII*, which encodes a formin protein that participates in spindle orientation by nucleating actin cables, or a deletion of *BIMI*, which encodes a protein that links microtubules to a myosin motor that walks along the actin cables (Pruyne et al., 2004). We chose to assay double mutants with *bni1Δ* and *bim1Δ* because genetic interactions involving *BNII* and *BIMI* have been well characterized (Tong et al., 2001) and the mutants have subtle defects in spindle function that appear mechanistically distinct.

We used automated image acquisition and analysis to quantify cell shape with respect to spindle morphology and score aberrant spindle defects (Fig. 1 A and Fig. S1; MetaXpress version 1.63, see Materials and methods). In brief, we used background fluorescence and a low threshold for GFP intensity to identify the individual cells or objects in each image (whole cell segmentation). Next, we identified spindles in the same image by varying the GFP threshold (spindle segmentation). After this, a minimal set of features such as area and shape factor were used to train the imaging software so that it could efficiently classify an unseen segmented image into two categories such as budded and unbudded cells. Each budded cell or unbudded cell was earmarked as a region of interest, and corresponding morphometric features were logged separately using the built-in functions of MetaXpress. An image-processing tool was then used to identify the bud neck region. After object identification, quantitative measurements allowed us to extract numerous morphometric features (Fig. S1) to generate a unique profile for each mutant strain (Tables S3–S5; see Materials and methods for more details on image analysis and morphometric feature extraction; for review see Vizeacoumar et al., 2009).

To identify genes that play a role in spindle dynamics, we concentrated on three basic spindle-specific features derived from the GFP-Tub1p reporter: (1) the ratio of spindle to cell length, (2) the orientation of the spindle with respect to the cell

axis, and (3) the distance between the center of the spindle and the bud neck. We assessed these features relative to cell cycle stage and searched for mutants that showed an altered distribution of cells for a given feature compared with wild type (see Materials and methods). For example, Fig. 1 B shows a 2D histogram of spindle orientation and budding index (cell cycle stage) for wild-type, *bim1Δ*, and *bni1Δ* cells. As expected, the *bim1Δ* culture showed a larger population of cells in the mid-upper region of the histogram (Fig. 1 B), representing cells that are in the medium-to-large budded stage with misoriented spindles. The distribution of *bni1Δ* cells was also deviant but more similar to that of wild-type cells due to a subtle spindle defect (Lee et al., 1999). Machine learning was used to classify the signal from the wild-type cells and used to rank the deviant mutants based on a significant p-value (see Materials and methods). Fig. 1 C shows the distribution of a collection of cells from two different mutant cultures: a control strain (*rcr2Δ*), which has normal spindle function, and *dyn2Δ*, a known spindle orientation mutant (Vallee et al., 2004). The budded cells examined from the mutant cultures are represented by a blue X and overlaid on the wild-type histogram. As expected, the *rcr2Δ* mutant fell into the wild-type category, with a p-value >0.1, whereas the *dyn2Δ* mutant was classified as having a spindle defect, with a p-value < 0.1.

Using a p-value cutoff of 0.1, we identified 1,962 mutants in our three screens as being defective in at least one of the three spindle-specific features (length, orientation, and distance to the bud neck). We applied a filter using 78 additional spindle-specific features, and by demanding a defect in at least 10 features, we honed our list to 745 mutants. Manual inspection confirmed obvious defects for 419/745 mutants (with a false negative rate of 44%). The known mutants that were missed using these criteria had p-values in the range of 0.1–0.5 and had significant p-values for some individual features.

To hone our list for more detailed analysis, we selected mutants with a highly penetrant nuclear positioning or delayed anaphase phenotype, the two most common defects seen in our screens. We also selected any mutants that showed a relatively rare bi-nucleation, spindle misorientation, or fish hook spindle phenotypes (Fig. 2). In this way, we selected 182 mutants from manual inspection for more detailed analysis; 92 genes were identified from screening the single mutant deletion array. We scored double mutants that enhanced spindle phenotypes relative to either the *bni1Δ* or *bim1Δ* single mutants and identified an additional 90 mutants. As expected, most mutants identified in the single mutant screen were also identified in the double mutant screens, and the *bni1Δ* and *bim1Δ* double mutant screens overlapped extensively, by 122 genes (Fig. 1 D). Analysis of gene ontology annotations revealed a clear enrichment for genes encoding proteins implicated in spindle-related processes, including genes with roles in microtubule-based processes ($P = 1.021 \times 10^{-14}$), tubulin folding ($P = 4.701 \times 10^{-10}$), cytoskeleton organization and biogenesis ($P = 5.702 \times 10^{-11}$), mitotic anaphase ($P = 9.394 \times 10^{-7}$), and chromosome segregation ($P = 7.699 \times 10^{-7}$), among others (Robinson et al., 2002). We also observed enrichment for genes with annotated functions in metabolism, ribosomal biogenesis, and RNA processing,

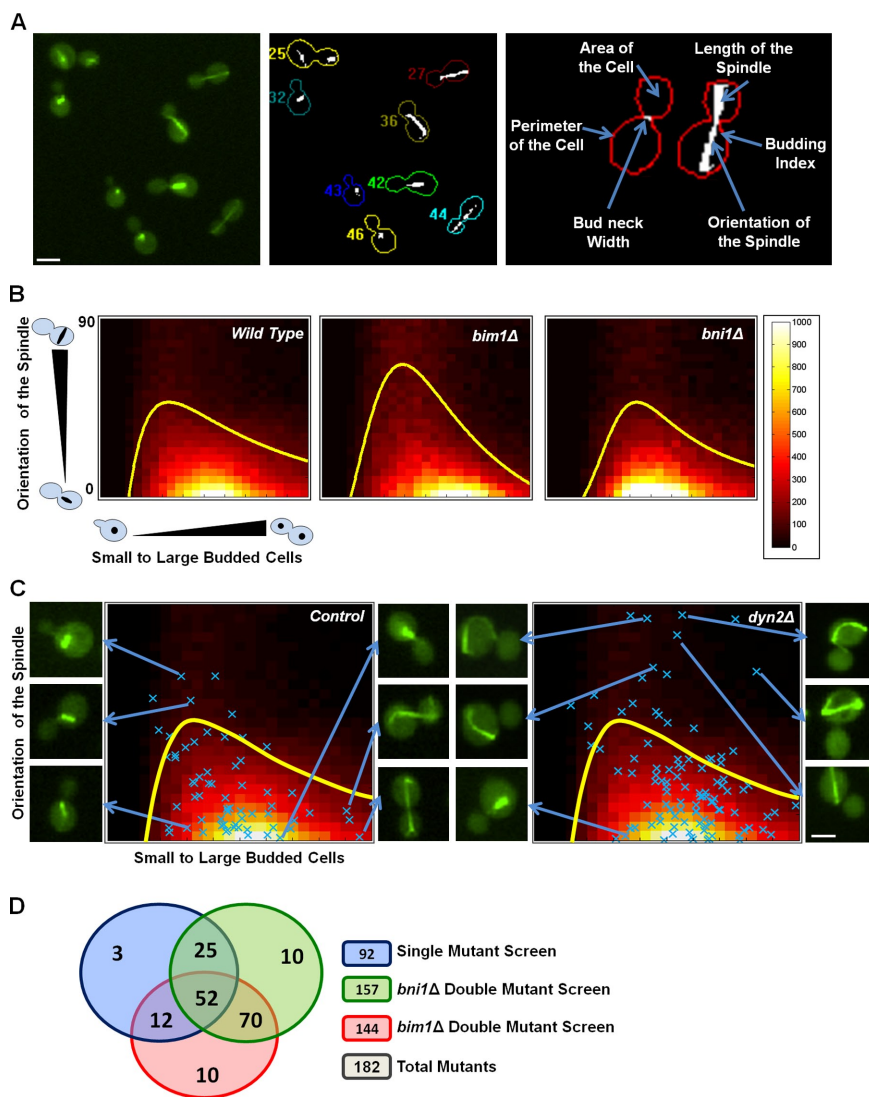


Figure 1. Automated image analysis and systematic identification of spindle-defective mutants using morphological profiles. (A) Illustration of image processing and segmentation approach. A representative fluorescent micrograph and corresponding segmented images from a high-content screen of cells expressing GFP-Tub1p are shown. The diagram on the right illustrates the attachment of specific labels to a region of interest (cell) to extract information for specific objects (the spindle) within the region. The numbers are automatically generated by the image analysis software. Bar, 5 μ m. (B) Heat maps showing distribution of wild-type, *bim1Δ*, and *bni1Δ* cells for spindle orientation. 2D histograms of the distribution of $\sim 35,000$ wild-type (left), and similar numbers of *bim1Δ* (middle) and *bni1Δ* (right) cells assessed for spindle orientation and budding index. The x axis represents the ratio of daughter to mother area (small to large budded cells) as an indication of cell cycle stage. The y axis represents the orientation of the spindle with respect to the orientation of the mother–bud axis of the cell. Colors on the heat map represent cell number as illustrated by the key to the right of the histograms. The yellow line is a contour line to indicate a boundary that contains the majority of the cells; with heat map representations, it is difficult to gauge the quantity of cells in lower density areas and some of the more subtle trends. To help visualize the overall trends in these heat maps and to make it easier to visually compare between the wild-type, *bim1Δ*, and *bni1Δ* plots, illustrative contour lines are plotted as yellow curves to indicate boundaries that roughly contain the majority of the cells below the curves. Given the binning of a 2D histogram, the curve is plotted so that the total number of cells in the bins above the curve is no more than 1,000, which is used so as to ignore the outliers with extreme spindle orientations. The curve is then smoothed by fitting the points using a linear/quadratic rational function. (C) Profiles of spindle orientation for *rcr2Δ* (control, left) or *dyn2Δ* mutant cultures. The distribution of ~ 60 – 100 budded cells from an *rcr2Δ* (control, left) or *dyn2Δ* mutant culture are represented by blue 'X's overlaid on an image of the 2D histogram from the wild-type culture (see B). Images corresponding to selected cells in each culture are shown. The increased representation of cells with misoriented spindles in the *dyn2Δ* mutant relative to the *rcr2Δ* culture is emphasized by the yellow contour line (see B). Axes are as in B. Bar, 5 μ m. (D) Venn diagram summarizing the number of mutants with aberrant spindle morphology identified by high-content screens of single and double deletion collections.

“X”s overlaid on an image of the 2D histogram from the wild-type culture (see B). Images corresponding to selected cells in each culture are shown. The increased representation of cells with misoriented spindles in the *dyn2Δ* mutant relative to the *rcr2Δ* culture is emphasized by the yellow contour line (see B). Axes are as in B. Bar, 5 μ m. (D) Venn diagram summarizing the number of mutants with aberrant spindle morphology identified by high-content screens of single and double deletion collections.

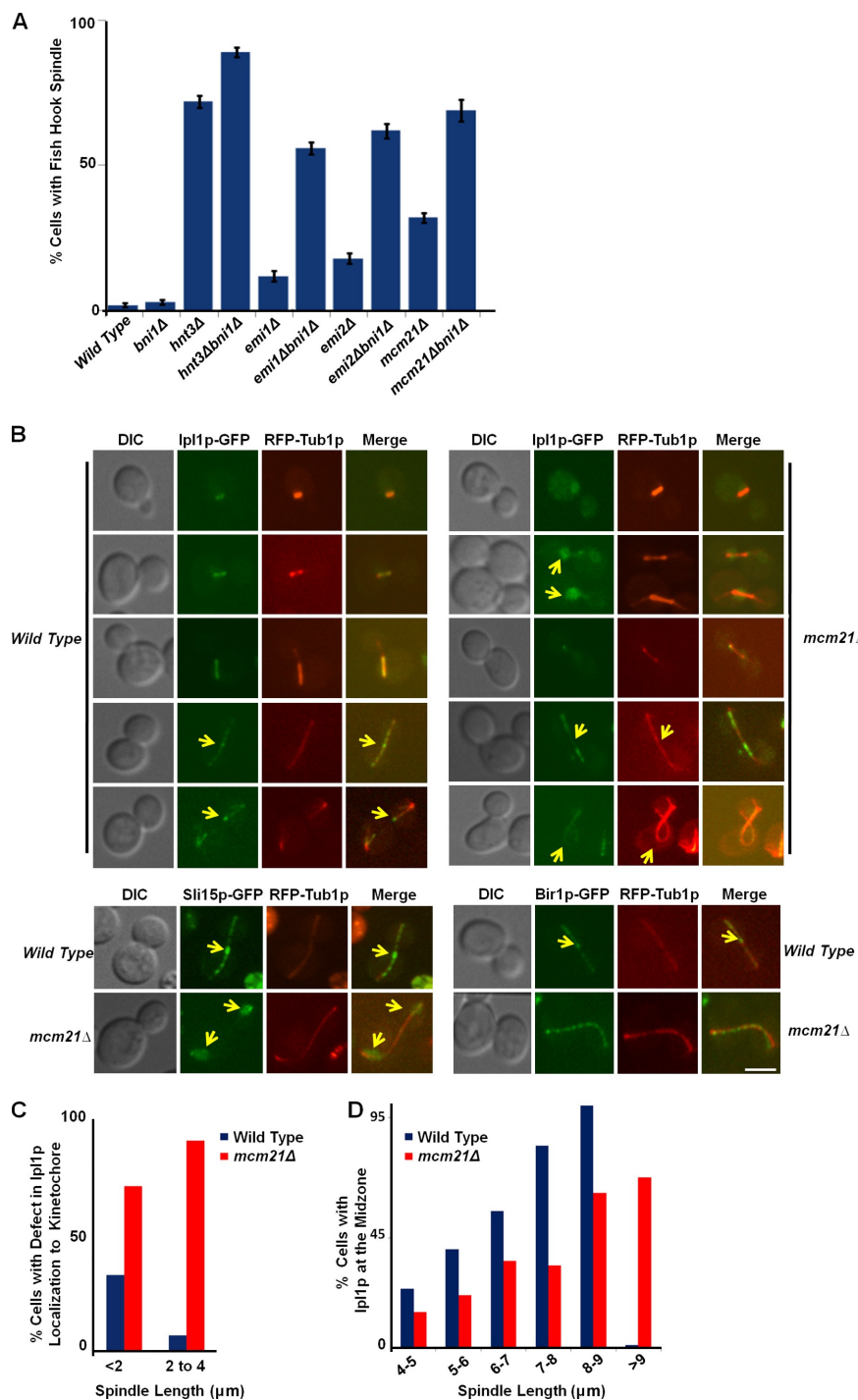
which is consistent with reported roles for nutrient signaling (Ras–cAMP pathway) and RNA-dependent protein complexes in regulating mitotic exit and mitotic spindle assembly, respectively (Morishita et al., 1995; Yoshida et al., 2003; Kittler et al., 2004; Blower et al., 2005).

To summarize the mutant phenotypes, we categorized each of the top-ranked mutants based on five major phenotypes by manual inspection (Fig. 2): (1) delayed nuclear positioning, in which the spindle fails to position close to the bud neck in medium/large budded cells; (2) delayed anaphase, in which the metaphase spindle persists in large budded cells; (3) bi-nucleated cells, where we observed two GFP dots, representing the spindle poles, within the mother of large budded cells; (4) misoriented spindle, in which the mitotic spindle is misaligned with the axis of the cell; and (5) fish hook spindle, in which the anaphase spindle is hyperelongated. Several genes with known roles in spindle dynamics were detected by our analysis, validating our

approach (Fig. 2). Although our method allows rapid assessment of deletion collections and the detection of many new spindle mutants, false negatives may occur because of a cell-sampling issue, especially if the single or the double mutants show a severe fitness defect. For example, some known spindle mutants were just below the cutoff range as assessed by the p-values generated (Table S6).

Novel candidate genes required for spindle disassembly

We identified a relatively rare subset of mutants that exhibited fish hook spindles, including five members of the CTF19 complex (*MCM21*, *MCM16*, *MCM22*, *CTF3*, and *CHL4*), which is associated with the yeast kinetochore. This hyper-extended spindle phenotype resembles that of spindle disassembly mutants defective for *IPL1*, which encodes the Aurora B kinase (Buvetot et al., 2003), or *KIP3*, which encodes a kinesin that



daughter cells after spindle disassembly (Fig. S2 A, red arrows), which is consistent with a loss of spindle pole polarity (Pereira et al., 2001) and consequent delay in cytokinesis (not depicted; Jensen et al., 2004). Time-lapse imaging also revealed cycles of partial elongation and collapse of the mitotic spindle without full elongation along the mother–bud axis in both *mcm21Δ* and *hnt3Δ* mutants (Fig. S2 A, blue arrows; and Fig. S2 F). Interestingly, we observed both the spindle instability and hyper-elongation phenotypes in the same cell (Fig. S2 A). We conclude that Mcm21p and Hnt3p may regulate both the stability of the growing anaphase spindle as well as spindle disassembly.

Ipl1p-GFP association with the spindle midzone is delayed in *mcm21Δ* cells

As noted earlier, yeast strains carrying mutations in the gene encoding the essential Aurora B kinase, *IPL1*, exhibit fish hook spindles, which is consistent with a role for Ipl1p in anaphase spindle disassembly (Buvelot et al., 2003). The products of *IPL1* (Aurora B), *SLI15* (IN-CENP), and *BIR1* (SURVIVIN) interact to form the chromosomal passenger complex (CPC), which performs key mitotic roles through dynamic relocation in a dividing cell (Zeng et al., 1999; Sullivan et al., 2001; Buvelot et al., 2003; Pereira and Schiebel, 2003; Ruchaud et al., 2007).

Figure 3. *hnt3Δ*, *mcm21Δ*, *emi1Δ*, and *emi2Δ* mutants have spindle elongation phenotypes and components of the CPC become partially mis-localized in *mcm21Δ* mutant cells. (A) Quantitation of number of cells with fish hook spindles in single and double mutant cultures. A histogram illustrating the percentage of cells in the indicated mutant cultures with fish hook spindles is shown. Cells were synchronized with α factor for 90 min, released into fresh medium, and assessed for fish hook spindles after 60 min; images of at least 100 anaphase cells for each culture were captured and quantified. Error bars show the standard deviation from three independent experiments. (B, top) Ipl1p-GFP localization to the elongating spindle and spindle midzone is disrupted in *mcm21Δ* mutant cells. Mid-log phase cells were treated with nocodazole for 2.5 h at room temperature and released into fresh medium before imaging. DIC images, fluorescent micrographs, and merged images are shown of representative single cells of wild-type (left) or *mcm21Δ* (right) strains expressing Ipl1p-GFP and RFP-Tub1p. Yellow arrowheads indicate the diffused localization of Ipl1p-GFP (for the *mcm21Δ* cells) and the spindle midzone. Bar, 5 μ m. (B, bottom) Sli15p-GFP is mislocalized, and Bir1p-GFP localization is unaffected in *mcm21Δ* mutant cells. Mid-log phase cells were treated with nocodazole for 2.5 h and released into fresh medium before imaging. DIC images, fluorescent micrographs, and merged images of a representative wild-type or *mcm21Δ* anaphase cell expressing Sli15p-GFP/Bir1p-GFP and RFP-Tub1p are shown. Yellow arrowheads indicate the localization of Sli15p-GFP. (C and D) Quantitation of the defect in Ipl1p-GFP localization at the kinetochore during metaphase and the spindle midzone during anaphase in wild-type and *mcm21Δ* mutant cells. (C) For kinetochore localization, cells with spindles between <2 and 2–4 μ m were quantified, as there was an increased mislocalization of Ipl1p-GFP/Sli15p-GFP during early anaphase. (D) For midzone localization, cells with spindles 4 μ m and longer were assessed. Cells with Ipl1p-GFP signal throughout the spindle were also considered as enriched for midzone in the quantitation. $n > 60$ –100 cells in each spindle length category.

Given that Mcm21p functions at the yeast kinetochore, we wondered whether the fish hook spindle defect in *mcm21Δ* mutants might be associated with mislocalization of Ipl1p. As expected, in wild-type cells, Ipl1p-GFP was localized to discreet dots at the kinetochore during metaphase, along the spindle as it elongated, at the midzone of the spindle during late anaphase, and finally to the trailing end of the disassembling microtubules (Fig. 3 B). In *mcm21Δ* cells, during metaphase, Ipl1p-GFP association with the kinetochore was reduced and remained diffusely localized throughout the nucleus (Fig. 3, B and C). During late anaphase, although Ipl1p appeared properly relocated to the spindle, we observed a delay in its spindle midzone accumulation (Fig. 3, B and D). Similar results were obtained for Sli15p-GFP (Fig. 3 B, bottom left). In contrast, Bir1p-GFP localized to the anaphase spindle normally in *mcm21Δ* cells with a mild delay (Fig. 3 B, bottom right), which is consistent with previous work suggesting that CPC components may have distinct functions (Gassmann et al., 2004; Thomas and Kaplan, 2007). These findings suggest that the fish hook phenotype in *mcm21Δ* cells may be caused by the mislocalization of the CPC, particularly the failure to localize Ipl1p to the spindle midzone. Consistent with our results, Knockleby and Vogel (2009) recently reported that Sli15p association with the kinetochore was reduced in mutants lacking the COMA complex, which is composed of Mcm21p and three other members of the CTF19 complex.

Genetic interactions involving *MCM21* and late mitotic regulators

Sli15p dephosphorylation at the kinetochore is necessary for the relocation of the CPC to the spindle midzone (Pereira and Schiebel, 2003). This reaction is mediated by the Cdc14p phosphatase, which is activated during early anaphase by the fourteen early anaphase release (FEAR) network proteins (Fig. 4 A). Although the release of Cdc14p from the nucleolus is initiated during early anaphase in a FEAR-dependent manner, maintenance of Cdc14p in the released state is controlled by the mitotic exit network (MEN) during the late stages of anaphase (Fig. 4 A; Buonomo et al., 2003; Pereira and Schiebel, 2003; Sullivan and Uhlmann, 2003; D'Amours and Amon, 2004). Ultimately, Cdc14p is resequenced back into the nucleolus concomitant with spindle disassembly after degradation of the Polo kinase Cdc5p, a key factor in releasing Cdc14p from its inhibitor in the nucleolus (Visintin et al., 2008).

To examine the functional relationship between Mcm21p and the FEAR network, we first tested for genetic interactions between *MCM21* and *SLK19*, which encodes a signaling component of the FEAR network (Fig. 4 A; Stegmeier et al., 2002; Pereira and Schiebel, 2003). The *mcm21Δ* and *slk19Δ* mutations combined to cause a more extreme double mutant phenotype in comparison to the corresponding single mutants. The *mcm21Δ slk19Δ* double mutant had a significant fitness defect, and ~90% of the anaphase cells exhibited severely coiled fish hook spindles (Fig. 4, B and C). This double mutant analysis highlights the critical roles of both the kinetochore and Cdc14p activation in spindle disassembly.

To generalize our conclusions, we examined spindle morphology in a panel of mutants defective for genes encoding

other components of the CTF19 complex, the FEAR network, and the MEN network. All the mutants we examined exhibited fish hook spindles to varying degrees (Fig. S3 A and Fig. 4 D). As previously described (Buvelot et al., 2003), we also found that mutant alleles of *IPL1* (*ipl1-1* and *ipl1-2*) were associated with a fish hook spindle phenotype (Fig. S3 A). Our observations combined with previous findings (Pereira and Schiebel, 2003; Stegmeier and Amon, 2004; Stoepel et al., 2005) suggest a model in which MEN and FEAR pathway components activate Cdc14p, which regulates the CPC after its docking at the kinetochore in a CTF19 complex-dependent manner.

Emi2p participates in Cdc14p activation

Because the MEN and FEAR networks control spindle disassembly, we asked if the fish hook spindle mutants that we identified in our screens might participate in these pathways. Emi2p is a possible MEN network component because affinity purification/mass spectrometry suggested an interaction with two MEN network proteins, Dbf2p and Lte1p (Graumann et al., 2004). Emi2p encodes a candidate hexose kinase (Johnston, 1999), which suggests a potential connection between nutrient sensing and cell cycle control. To assay for a functional linkage between Emi2p and the MEN or FEAR pathway, we made *emi2Δ* double mutants with deletion alleles of genes encoding either MEN or FEAR components. Double mutants combining *emi2Δ* with deletion alleles of either MEN (*lte1Δ*, *dbf2Δ*) or FEAR (*bns1Δ*, *spo12Δ*, *slk19Δ*) components showed an exaggerated fish hook spindle (Fig. 4 D and Fig. S3 B). An *emi2Δ dbf2Δ* double mutant strain was inviable, providing genetic evidence that Emi2p may function in parallel with *DBF2*, perhaps in the FEAR pathway (unpublished data). These genetic data, and the possible physical interaction between Emi2p and MEN components, suggest involvement of Emi2p in both the MEN and FEAR networks.

To contrast these observations, we also examined genetic conditions that activate the MEN network. Bub2p and Bfa1p are inhibitors of MEN and the subsequent release of Cdc14p, as they form a GTPase-activating complex (GAP), or an inhibitor for the Tem1p GTPase (Fesquet et al., 1999; Pereira et al., 2000; Geymonat et al., 2002; Ro et al., 2002). In the *emi2Δ bub2Δ* double mutant, the anaphase spindles extended normally, and cells underwent mitosis like wild-type cells (Fig. 4 D and Fig. S3 B). Consistent with this finding, overexpression of *MOB1*, an activating MEN component, also rescued the fish hook spindle in *emi2Δ* cells (Fig. 4 D). Thus, defects in MEN and FEAR signaling accentuate the *emi2Δ* mutant phenotype, whereas activation of the MEN pathway appears to suppress it. Finally, we examined Cdc14p localization in *emi2Δ* cells to evaluate its role in Cdc14p release. Wild-type cells largely release Cdc14p from the nucleolus as the spindles start to elongate, and, concomitant with spindle disassembly, they resequence Cdc14p back into the nucleolus (Stegmeier et al., 2002; Visintin et al., 2008). In contrast, the phenotype of *emi2Δ* cells resembled that of *dbf2Δ* mutants; ~21% of the cells showed Cdc14p-GFP resequenced back into the nucleolus even before spindle disassembly (Fig. 4, E and F, blue arrows). Thus, like mutants in the MEN and FEAR network genes, *emi2Δ* cells appear to have a defect in

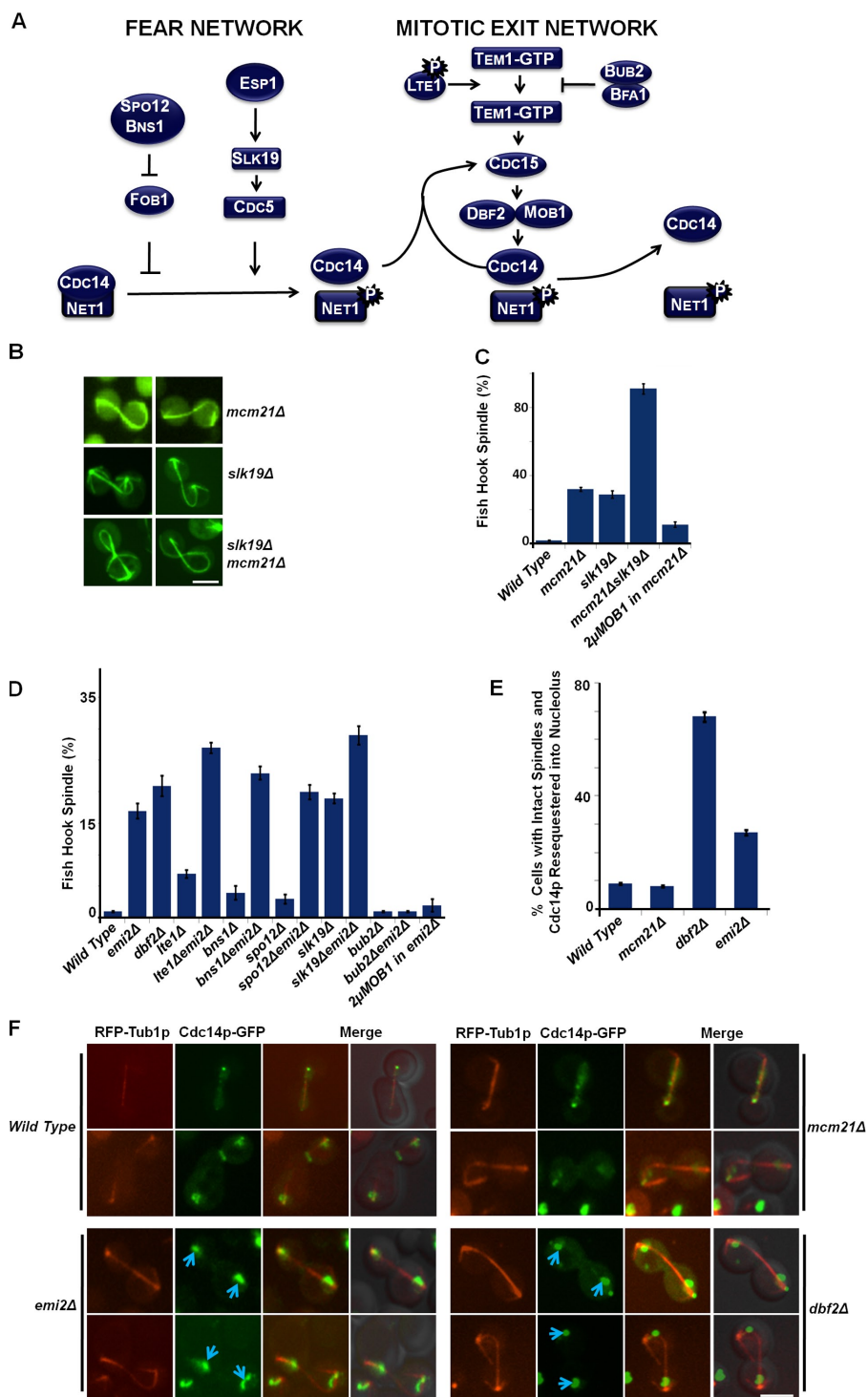


Figure 4. Genetic interactions involving the FEAR network, MEN, and kinetochore components. (A) Diagram of key components of the FEAR network and MEN. Cdc14p is released from the nucleolus during early anaphase by the FEAR network and maintained in a released state by the MEN proteins. (B) Exacerbation of the fish hook spindle phenotype of *mcm21Δ* mutant cells by deletion of a FEAR network activator. Representative fluorescence micrographs of GFP-Tub1p in *mcm21Δ*, *slk19Δ*, and *slk19Δ mcm21Δ* cells are shown. Bar, 5 μ m. (C) Quantitation of the fish hook spindle phenotype for the mutants shown in B. The plot shows the percentage of anaphase cells for the indicated mutant cultures with a clear fish hook spindle phenotype. Quantitation of the defect in an *mcm21Δ* mutant overexpressing *MOB1* is also shown. Error bars show the standard deviation from three independent experiments counting \sim 100 cells for each strain. (D) Quantitation of the fish hook spindle phenotype for single and double mutants of *EMI2* with FEAR and MEN components. The plot shows the percentage of anaphase cells for the indicated mutant cultures with a clear fish hook spindle phenotype. Error bars show the standard deviation from three independent experiments counting \sim 100 cells for each strain. (E) Quantitation of the percentage of cells with intact spindles that show premature resequstration of Cdc14p-GFP into the nucleolus. Cells were synchronized using α factor, released into fresh medium, and monitored using live-cell imaging every 15 min for 180 min. RFP-Tub1p was used to monitor the spindle and identify the cell cycle stage. Error bars show the standard deviation from three independent experiments counting \sim 80 cells for each strain in all the time points. (F) Release of Cdc14p-GFP in *mcm21Δ*, *emi2Δ*, and *dbf2Δ* mutant cells. Cells were synchronized using α factor, released into fresh medium, and monitored using live-cell imaging every 15 min for 180 min. RFP-Tub1p was used to monitor the spindle and identify the cell cycle stage. Representative wild-type, *emi2Δ*, *mcm21Δ*, and *dbf2Δ* mutant cells in late anaphase are shown. Blue arrows indicate the premature sequestration of Cdc14p to the nucleolus before spindle disassembly. Note that unlike *emi2Δ* and *dbf2Δ* cells, *mcm21Δ* cells maintained the released state of Cdc14p even when the spindle was hyperelongated. Bar, 5 μ m.

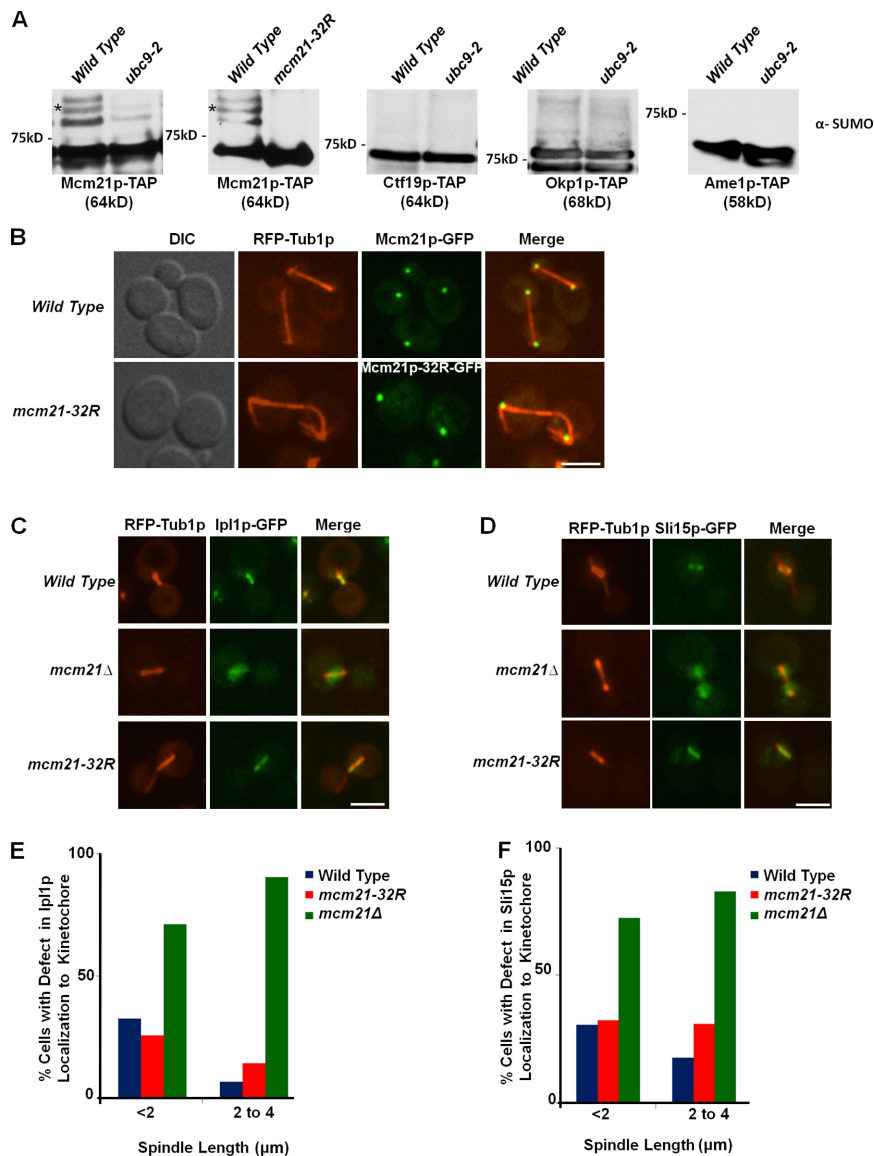
maintaining Cdc14p in an active released state, which suggests that Emi2p may modulate one of these pathways.

Sumoylation of Mcm21p targets the CPC specifically to the spindle midzone

In addition to the nonessential gene set, we also screened a collection of temperature-sensitive mutants covering \sim 100 essential genes for defects in spindle morphology (Table S7). By screening this collection, we identified a spindle disassembly defect (fish hook spindle) associated with a mutant allele of *MMS21*

(Fig. S3 A), which encodes one of the known E3 SUMO ligases (Zhao and Blobel, 2005). We were intrigued by this observation because recent work from our laboratory identified genetic interactions between *MCM21* and genes encoding SUMO pathway components, which suggested a link between sumoylation and Mcm21p function (Makhnevych et al., 2009). Mcm21p is the only protein in the CTF19 complex that is known to be sumoylated (Panse et al., 2004; Wohlschlegel et al., 2004; Zhou et al., 2004; Denison et al., 2005; Hannich et al., 2005; Wykoff and O'Shea, 2005), raising the possibility that sumoylation may

Figure 5. Sumoylation of Mcm21p is not required for kinetochore localization of the CPC. (A) Sumoylation of CTF19 complex components. Immunoprecipitation/Western blotting was performed from protein extracts of wild-type or *ubc9-2* strains expressing Mcm21p-TAP, Ame1p-TAP, Ctf19p-TAP, or Okp1p-TAP. A strain expressing a version of TAP-tagged Mcm21p lacking 32 lysine residues (*mcm21-32R*) was also analyzed for SUMO modification. The asterisk indicates sumoylated Mcm21p protein. The anti-SUMO antibody detects both sumoylated and unmodified proteins due to the associated TAP tag. (B) Subcellular localization of wild-type Mcm21p-GFP and Mcm21p-32R-GFP. DIC images, fluorescent micrographs, and merged images of representative wild-type or *mcm21Δ* anaphase cells expressing either wild-type Mcm21p-GFP or Mcm21p-32R-GFP and RFP-Tub1p are shown. Note the formation of a fish hook spindle in the *mcm21-32R* mutant background. Bar, 5 μ m. (C and D) Ipl1p-GFP (C) and Sli15p-GFP (D) localization to the kinetochore in wild-type, *mcm21-32R*, and *mcm21Δ* mutant cells. Mid-log phase cells were treated with nocodazole for 2.5 h at room temperature and released into fresh medium before imaging. Fluorescent micrographs and merged images are shown of representative single cells of wild-type, *mcm21Δ*, or *mcm21-32R* strains expressing Ipl1p-GFP and RFP-Tub1p. Bar, 5 μ m. (E and F) Quantitation of the defect in Ipl1p-GFP (E) or Sli15p-GFP localization to the kinetochore during metaphase in wild-type, *mcm21Δ*, and *mcm21-32R* mutant cells. Cells with spindles between <2 and 2–4 μ m were quantified for Ipl1p-GFP (E) or Sli15p-GFP localization to the kinetochore (F) as indicated. $n > 200$ cells in each spindle length category.



regulate CPC localization and that the sumoylation of Mcm21p may be regulated by the E3 ligase *MMS21*. Consistent with this idea, two observations suggested that factors in addition to Cdc14p influenced CPC localization in the *mcm21Δ* mutant. First, unlike *emi2Δ* cells, we found that the kinetics of Cdc14p localization were unaffected in *mcm21Δ* cells, yet Ipl1p-GFP failed to properly localize to the spindle (Fig. 4 F and Fig. 3 B). Second, hyperactivation of the Cdc14p signaling pathway through overexpression of a MEN component, *MOB1* (Komarnitsky et al., 1998), resulted in only partial rescue of either the Ipl1p-GFP mislocalization phenotype or the fish hook spindle phenotype (Fig. 4 C and Fig. S3, C and D). These findings indicate that signaling from Cdc14p alone is not sufficient to target the CPC to the spindle midzone, which suggests that Mcm21p might play additional roles at the kinetochore.

We explored this idea by first assessing Mcm21p and its closely associated CTF19 complex proteins Okp1p, Ame1p, and Ctf19p (the COMA subcomplex), and confirmed that only Mcm21p was detectably sumoylated in our assay (Fig. 5 A).

To dissect the role of Mcm21p sumoylation in spindle function, we first mutated the best matches to the consensus site for sumoylation in Mcm21p (Jeram et al., 2009), and observed no significant effect on Mcm21p sumoylation (unpublished data). Because >40% of the published yeast SUMO conjugation sites occur at nonconsensus lysine residues (Jeram et al., 2009), we next synthesized a sumoylation-deficient allele of *MCM21*, *mcm21-32R*. We made mutations that changed all 32 Mcm21p lysine residues to arginine (Mcm21p-32R), and we examined the functionality of the Mcm21p-32R mutant in three different ways. First, we found that the Mcm21p-32R mutant was expressed at normal levels but was not sumoylated (Fig. 5 A). Second, when expressed as a GFP chimera, Mcm21p-32R localized normally to the kinetochore (Fig. 5 B). Third, tetrad dissection revealed that expression of *MCM21-32R* rescued the synthetic lethality of a *mcm21Δ mad1Δ* double mutant strain (unpublished data).

Unlike in the *mcm21Δ* deletion mutant, the kinetochore association of Ipl1p-GFP and Sli15p-GFP was not affected during metaphase in the *mcm21-32R* mutant, which suggests

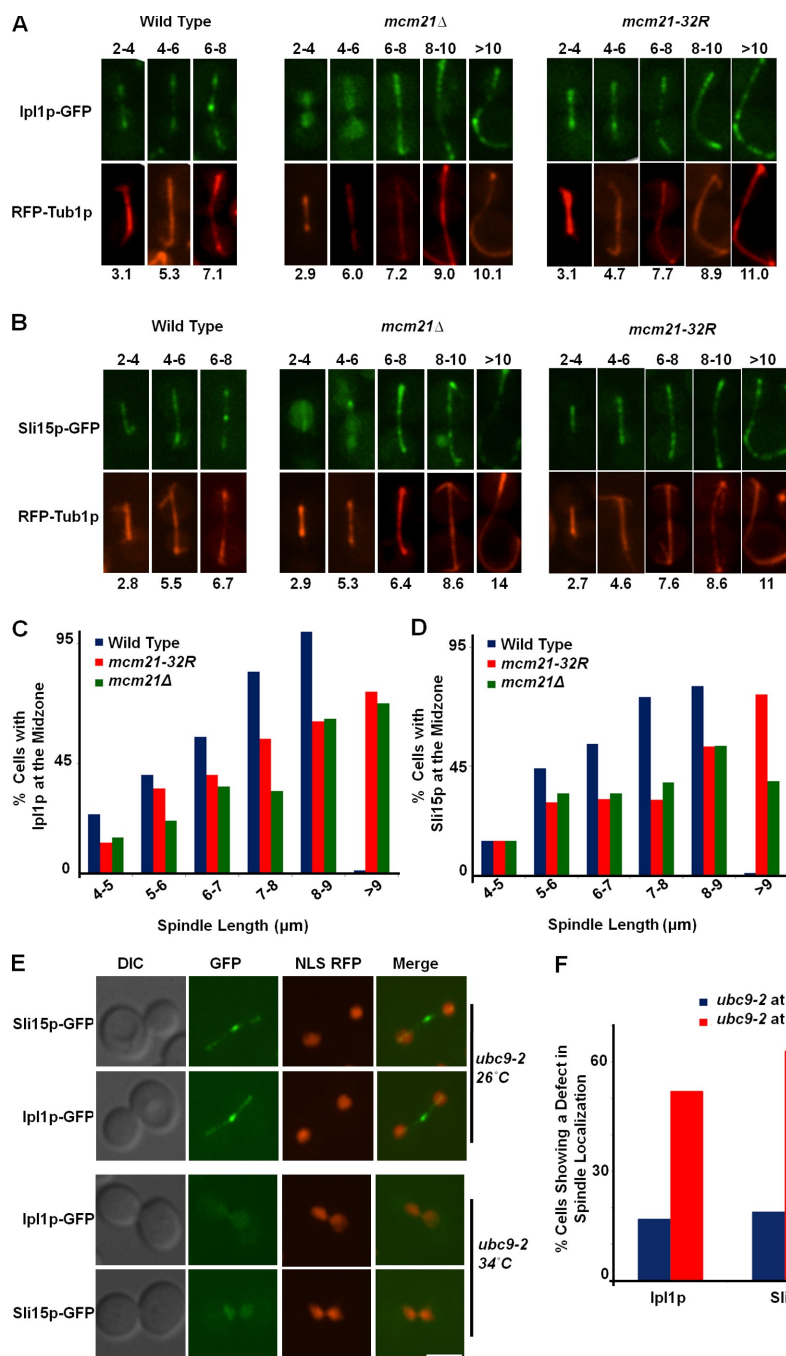


Figure 6. Sumoylation of Mcm21p regulates the localization of the CPC to the spindle midzone. (A and B) Ipl1p-GFP and Sli15p-GFP localization to the spindle midzone in wild-type, *mcm21-32R*, and *mcm21Δ* mutant cells. Mid-log phase cells were treated with nocodazole for 2.5 h at room temperature and released into fresh medium before imaging. Fluorescent micrographs of representative single cells of wild-type, *mcm21Δ*, or *mcm21-32R* strains expressing Ipl1p-GFP (A), Sli15p-GFP (B), and RFP-Tub1p are shown. Numbers at the top of each panel denote the spindle length (μm) range that each micrograph represents, and the numbers at the bottom represent the spindle length (μm) of the cell shown. (C and D) Quantitation of the defect in Ipl1p-GFP and Sli15p-GFP localization to the spindle midzone in wild-type, *mcm21Δ* mutant cells, and *mcm21-32R* mutant cells. Cells with spindles 4 μm and longer were used to quantify Ipl1p-GFP (C) or Sli15p-GFP (D) localization to the spindle midzone as indicated. $n > 60$ –100 cells in each spindle length category. Cells with Ipl1p-GFP or Sli15p-GFP signal throughout the spindle were also counted as mid-zone enriched for the quantitation. (E) Localization of Ipl1p-GFP and Sli15p-GFP in *ubc9-2* strains. Cells were grown at 34°C for 3 h and imaged immediately (34°C panels) or shifted to 26°C for 2 h before samples were imaged (26°C panels). DIC images, fluorescent micrographs, and merged images are shown of representative single cells. Bar, 5 μm. (F) Quantitation of the defect in spindle localization of Ipl1p-GFP and Sli15p-GFP for mutants represented in E. $n > 100$ cells.

that Mcm21p-32R still retains the scaffolding function associated with wild-type Mcm21p at the kinetochore (Fig. 5, C–F). Nevertheless, like the *mcm21Δ* deletion mutant, the *mcm21-32R* mutant was defective for targeting Ipl1p-GFP and Sli15p-GFP to the spindle midzone, resulting in the formation of extended fish hook spindles (Fig. 6, A–D). Wild-type cells were able to target Ipl1p-GFP and Sli15p-GFP to the midzone, such that the spindle reached a maximum length of 6–8 μm before disassembly, whereas the *mcm21Δ* and the *mcm21-32R* mutant cells were defective in this localization and showed an extended fish hook spindle that often grew beyond 9 μm (Fig. 6, A–D). Invariably, every cell that formed a fish hook spindle did not localize Ipl1p-GFP to the midzone in both the *mcm21Δ* deletion mutant

and the *mcm21-32R* mutant, which suggests that sumoylation of Mcm21p may signal the efficient relocation of the CPC to the spindle midzone.

To further assess the role of sumoylation in CPC localization, we examined a *ubc9-2* temperature-sensitive mutant defective for the SUMO E2 ligase. Sumoylation is involved in many cellular processes (Melchior, 2000; Müller et al., 2001; Seeler and Dejean, 2003), and most *ubc9-2* mutant cells arrest in metaphase and early anaphase (Fig. 6 E), precluding analysis of the fish hook spindle phenotype. Nonetheless, the large budded *ubc9-2* cells clearly failed to efficiently localize both Ipl1p-GFP and Sli15p-GFP to the spindle at the restrictive temperature (Fig. 6, E and F). After release from the restrictive temperature,

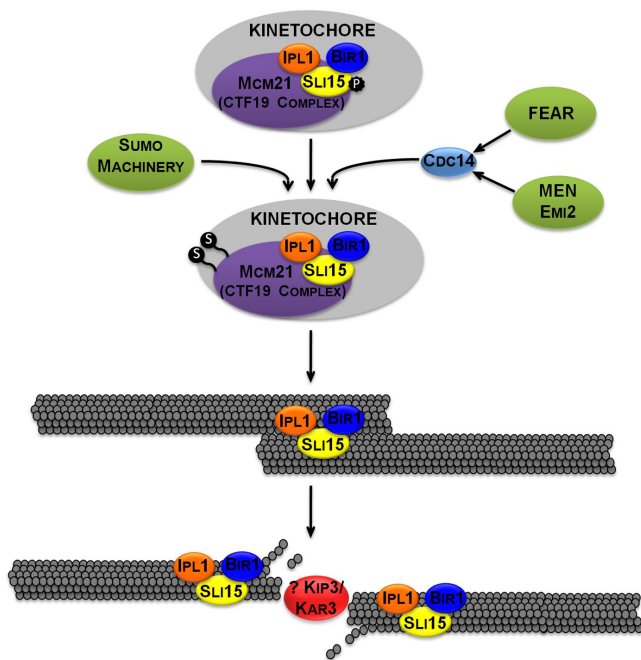


Figure 7. Model of mitotic exit and spindle disassembly. Major regulators of the CPC during mitosis are illustrated. For simplicity, MEN and FEAR pathway components are not shown. FEAR activates the partial release of Cdc14p during early anaphase, and MEN activates the complete release of Cdc14p during late anaphase. Cdc14p release from the nucleolus and sumoylation of Mcm21p at the kinetochore seem to be two important signals that regulate the dynamic relocation of the CPC components to the spindle midzone from the kinetochore. We suggest that Mcm21p along with the members of the CTF19 complex may act as a scaffold for the CPC. Specifically, in cooperation with Cdc14p, sumoylation of Mcm21p may increase the efficiency of timed localization of the CPC to the spindle midzone for proper disassembly of the spindle.

Ipl1p-GFP rapidly enriched along the spindles and specifically concentrated at the spindle midzone as expected (Fig. 6 E). Thus, sumoylation of Mcm21p appears to play a specific role in targeting the CPC to the spindle midzone.

Discussion

Integrating SGA analysis and HCS provides a general strategy for quantitative assessment of cell biological phenotypes on a genome-wide scale in sensitized genetic backgrounds. Automation and machine learning techniques are required to scale this analysis to multiple pathways, enabling objective, quantitative, and highly reproducible determination of detailed morphological phenotypes. Although the deletion collection has been assessed for morphological phenotypes through systematic analysis of fixed cells (Ohya et al., 2005), our study represents the first fully automated genome-scale mutant screen tracking a dynamic intracellular event. An unbiased quantitative readout allows for the identification of subtle but significant phenotypes, offering the potential to confirm and expand genetic networks based solely on fitness measurements. For example, with a *BIM1* query mutation and combined SGA-HCS system, we scored 45 genes (~50%) previously identified as *BIM1* synthetic lethal-sick interactions (Tong et al., 2004), but we also identified 122 novel genes involved in spindle function. A limitation

of our system is that true synthetic lethal double mutants fail to divide and cannot be examined by HCS (Fig. S4 A); however, this problem can be overcome if the double mutant is made conditional, as through the use of a temperature-sensitive allele of one member of the gene pair (Xu et al., 2007).

Morphological mutants, networks, and complexes

We compared our phenotypic profiling results to genetic and protein-protein interaction datasets, and found that mutant strains that had a high phenotypic deviation from wild type were more likely to be highly connected in the existing synthetic lethal genetic and protein-protein interaction networks (Fig. S4, B and C). Thus, an accurate assessment of phenotypic deviance from wild type may allow us to infer participation of proteins or genes in network hubs (Rutherford and Lindquist, 1998). The occurrence of a specific phenotypic change in response to a particular mutation was also correlated for proteins within the same complex (Fig. S4 D). For example, we observed that members of the CTF19 complex exhibit a similar fish hook spindle phenotype, as do components of the FEAR and MEN pathways (Fig. S3 A).

Spindle disassembly pathway

Our large-scale analysis of mutants displaying a fish hook spindle combined with previous observations elaborate a general model of spindle disassembly in yeast (Fig. 7; Pereira and Schiebel, 2003; Stegmeier and Amon, 2004; Stoepel et al., 2005). In particular, our study established a new role for sumoylation at the kinetochore associated with the CTF19 complex and modulation of spindle disassembly. We suggest that Mcm21p along with the members of the CTF19 complex may act as a scaffold for docking the CPC at the kinetochore. Our data suggest that signaling from Cdc14p alone is not sufficient and that sumoylation of Mcm21p is necessary for the movement of Ipl1p from the kinetochore to the spindle midzone. Alternatively, it might be that sumoylation could trigger release of Ipl1p from the kinetochore. This might facilitate Cdc14p-dependent dephosphorylation of Sli15p and the subsequent targeting of Ipl1p to the spindle midzone. This is evident from the observation that Ipl1p stably associates with the spindle in the *mcm21-32R* mutant, which suggests that the dynamic relocation of Ipl1p is tightly regulated, presumably to avoid premature spindle disassembly.

We also discovered that Emi2p, a hexose kinase family member, is involved in the activation of Cdc14p. Hexose kinases participate in carbon sensing (Johnston, 1999), but several observations suggest an additional role for these enzymes in cytoskeletal regulation. For example, binding assays and electron microscopic studies revealed binding of bovine brain hexose kinase (HK1) to microtubules (Wagner et al., 2001). Also, hexose kinases may regulate the movement of kinesin motors on microtubules by quenching ATP molecules (Hess et al., 2001). Our observations, coupled with these results, suggest a possible role for Emi2p in linking nutrient sensing to mitotic exit. An *emi2Δ dbf2Δ* double deletion mutant is synthetic lethal, which suggests that Emi2p may play a role in the parallel FEAR

pathway. However, the reported physical interaction of Emi2p with MEN components suggests that Emi2p may also be involved in the MEN pathway (Graumann et al., 2004). Genetic analyses of pathway components suggest that if we delete two nonessential components of a pathway containing at least one essential component, synthetic lethality is expected between the nonessential components (Bandyopadhyay et al., 2008). Accordingly, we suggest that Emi2p is a novel member of the MEN pathway.

Interestingly, Cdc14p is required for anaphase spindle stabilization (Khmelninskii et al., 2007; Khmelninskii and Schiebel, 2008), yet spindle disassembly defects are invariably found in all FEAR and MEN mutants (Toyn and Johnston, 1994; Jensen et al., 2004; Stoepel et al., 2005). Consistent with these observations, roles for Cdc14p in both meiotic and mitotic spindle disassembly have been described (Buvelot et al., 2003; Marston et al., 2003). Both Cdc14p and Ipl1p have several roles within the cell, and current literature suggests that there is a qualitative and quantitative difference in the Cdc14p released from the FEAR and MEN pathways (Stegmeier and Amon, 2004). Accordingly, Cdc14p released from the FEAR may stabilize the spindle, whereas Cdc14p released from the MEN may destabilize the spindle.

Although we used spindle morphology as a proof-of-principle, combining SGA analysis and HCS enables virtually any pathway that can be monitored with a fluorescent reporter to be assessed quantitatively within the context of numerous genetic and environmental perturbations. In theory, this general system should enable the yeast community to collect a wealth of quantitative HCS datasets under standardized formats. The potential for integration of hundreds of combined SGA-HCS analyses offers the possibility of a new global view of the cell.

Materials and methods

Automated image acquisition

A modification of the SGA method (Tong et al., 2001; Sopko et al., 2006) was used to introduce the GFP-Tub1p-expressing plasmid and the deletion allele of *BNI1* into the deletion array. A strain harboring *bni1Δ* (Table S2) was transformed with a GFP-Tub1p plasmid and mated to the yeast deletion array (Giaever et al., 2002) by replica pinning. Diploids were selected and sporulated using standard SGA selections (Tong et al., 2001). *MATa bni1Δ genexΔ* haploids expressing GFP-Tub1p were isolated through successive pinning onto selective media and then into liquid selection medium for overnight growth. To optimize cell density for image analysis, we used liquid-handling robots (Biomek FX Laboratory automation work station; Beckman Coulter) to dispense sample volumes based on the optical density of each strain (SpectraMax Plus 384 Microplate Spectrophotometer; MDS Analytical Technologies). Plates were imaged in 96-well format using glass-bottomed plates (MMI Greiner M plates), and each plate contained control strains at 19 positions amounting to ~1,064 controls per screen. A fluorescence microscopy system (ImageXpress 5000A; MDS Analytical Technologies) was used to acquire images. Images were acquired with 60x dry objective (Plan-fluor) with an NA of 0.85 and a working distance of 370 μm. Images were acquired at room temperature unless indicated using a 1,280 × 1,024 cooled charge-coupled device camera with 12-bit readout. Low fluorescent media (Sheff and Thorn, 2004) was used to resuspend the cells before imaging. To increase the throughput, we linked automated incubators (Cytomat; Thermo Fisher Scientific) to the Image Express system to allow automated loading of plates into the imager using a robotic arm (CRS Catalyst Express; Thermo Fisher Scientific) and integration software (Polara; Thermo Fisher Scientific).

Automated image analysis

Automated image acquisition and analysis were performed with MetaXpress software version 1.63 (MDS Analytical Technologies). After images were shade-corrected and background-subtracted, objects were segmented

and single cells were defined using background cell fluorescence in the GFP channel. We used a series of MetaXpress modules to segment whole cells as well as objects inside cells. The segmented images were then binarized to produce three files for each image: entire cells, spindle objects, and the bud neck regions (Fig. S1). Once cells were identified, dead cells were removed from further analysis by gating average grayscale, as they had high autofluorescence. Then a minimal set of features (dimension, shape factor, and elliptical form factor) were used to train the software to efficiently classify an unseen image into two categories such as budded and unbudded cells. Each budded or an unbudded cell was taken as a region of interest, and the morphometric features of each region of interest and relevant objects (spindle) were quantified individually for each cell. Water shedding was used to identify the bud neck region, and several morphometric readouts for the mother and daughter portions of the cells were also generated using the built-in options of MetaXpress.

We measured several morphometric characteristics of each cell and the spindle, applying appropriate statistical measurements. By dimensionality reduction (Kaufman and Rousseeuw, 1990), we chose 77 nonredundant "geometric features", each of which contained four statistical parameters (mean, variance, minimum value, and maximum value). We also considered 13 features that calculate percentage values because of their biological relevance (for example, percentage of large budded cells with an anaphase spindle). Thus, the morphological profile of each strain includes 321 cellular measurements, 240 of which were attributed to cell morphology and 81 attributed to spindle morphology (Tables S3–S5; cataloged measurements are summarized in Table S1). Our measurements include a description of cell shape, a feature that can serve as a proxy for cell cycle position (unbudded, small budded, medium budded, and large budded cells), characteristics of spindle pole bodies, and the mitotic spindle. The cataloged measurements in Tables S3–S5 are a mean of all the values measured in each mutant.

Data analysis

To identify mutants whose morphological profiles differed from wild type, we used a mixture of Gaussian models to learn the probability density function of the control based on the four features (Bishop, 2006). The mother-daughter cell size ratio is used in the analysis as an indication of cell cycle stage (Byers and Goetsch, 1975; Kilmartin and Adams, 1984). Cross-validation revealed that 60 Gaussians was optimal for this dataset. Mutant strains were evaluated by computing the likelihood under this learned model. A low likelihood indicates that the cells of the mutant strain exhibit phenotypes noticeably different than that of the control. Because the number of identified and measured cells differs for each strain, the likelihoods must be normalized to compare the different strains as well as provide a measure of statistical significance. So for a strain with a sample size of n cells, a random sample of n cells from the mixture of Gaussians was drawn, and the likelihood of these randomly drawn cells was computed. This sampling procedure was conducted 2,000 times, and the likelihood of the mutant cells was compared with the likelihood of the random samples to provide a p-value for the mutant phenotype. The same procedure was applied to other measurements to find mutant strains for different phenotypes as well as for double knockout experiments.

To assess the correlation between gene connectivity and phenotype, we downloaded all available synthetic lethal interaction data from BioGrid (<http://www.thebiogrid.org/>) and protein-protein interaction data from the Database of Interacting Proteins (<http://dip.doe-mbi.ucla.edu/>). We identified the top 100 highly connected genes and the bottom 100 least-connected genes in each of these datasets. The mean phenotypic change and the 95% confidence interval of the mean are derived from 5,000 bootstrap resamplings. P-values were derived using a Mann-Whitney U test. Fig. S4 (B and C) shows the mean phenotypic alterations in these gene datasets. Mean phenotypic variation is defined as the mean number of altered morphometric measurements; for each gene, we counted the number of altered phenotypic features for both the single deletion and the double deletion. To determine whether or not the loss of proteins in the same complex tends to cause similar morphology profiles, we compared phenotypic correlation within complexes against random controls. A total of ~274 literature-curated protein complexes and a similar set of randomly generated protein complexes were examined for the correlation of their morphological profile. Phenotypic correlation is defined as the mean pairwise correlation among complex subunits. We evaluated phenotypic correlation upon deletion of genes involved in the same protein complexes. In brief, we calculated pairwise Pearson's correlation for genes involved in protein complexes, and mean pairwise correlation was then compared against a set of random

controls in which complex memberships were randomly shuffled. Fig. S4 D shows the correlation between true complexes and random complexes.

Confocal microscopy and image quantitation

Images were captured using a spinning disc confocal system (WaveFX; Quorum) with an ultra-cooled 512 back-tinned EM charge-coupled device camera, or a microscope (E-600FN; Nikon) with an Orca camera (Hamamatsu). Images were acquired with 63× HCX Plan-Apochromat oil objective with an NA of 1.4. Images were captured at room temperature after loading the cells on gelatin pads as described previously (Jones et al., 1993; Yeh et al., 1995). Stacks of 11 optical sections spaced 0.3 μm apart or 5 optical planes spaced 0.2 μm apart were captured every 1 min. GFP was excited using a 488-nm laser, and its emission was collected using a 505-nm long-pass filter. No further processing was needed, as raw images clearly showed the phenotype. The z-axis images were converted to a single composite image by using the brightest pixel at every position in each of the image planes. This maximum pixel projection technique produced a 2D representation of the GFP fusion proteins within the cell from the 3D dataset. A macro written with the MetaMorph scripting language was used to input the entire stack of background-subtracted images and output a new stack of only the projected images, and to measure the spindle length in every z-stack plane.

Detection of SUMO conjugates and Western blot analysis

The *mcm21-32R* mutant was made by gene synthesis (DNA2.0, Inc.). The mutated gene (1,190 bp) and its associated promoter (500 bp), with a C-terminal tandem affinity purification (TAP) tag (543 bp) and downstream sequences (200 bp), were cloned into the BamHI and HindIII sites of the pRS315 vector. To construct the *mcm21-32R-GFP*, the mutated gene was amplified with appropriate primers and integrated into the genome along with a GFP tag. wild-type or *ubc9-2* strains expressing TAP-tagged versions of Mcm21p, Ctf19p, Ame1p, and Okp1p were grown in YPD to an OD₆₀₀ of 0.4 at 25°C, then the temperature was shifted to 34°C for 3 h. Cells were collected by centrifugation and lysed by bead beating in 10% glycerol, 50 mM Hepes-KOH, pH 8.0, 0.1 M KCl, 2 mM EDTA, 0.1% NP-40, 2 mM DTT, 10 mM N-ethylmaleimide, and yeast protease inhibitor cocktail (Sigma-Aldrich). Samples were clarified by centrifugation (16,000 g for 5 min at 4°C), and TAP-tagged proteins were isolated using mouse IgG beads (Dynabeads; Invitrogen). Beads were washed extensively with wash buffer containing 0.25 M MgCl₂, and bound proteins were eluted with Laemmli buffer. Specific rabbit polyclonal antibodies were used to detect Smt3p (Rockland Immunochemicals, Inc.). TAP-tagged proteins were detected with normal rabbit serum.

Online supplemental material

Fig. S1 shows steps involved in automated image analysis. Fig. S2 shows quantitation of spindle length defects in *hnt3Δ*, *mcm21Δ*, *emi1Δ*, and *emi2Δ* single and double mutant strains. Fig. S3 shows representative micrographs of fish hook spindle mutants. Fig. S4 shows correlation of the phenotypic changes in single mutant and *bni1* or *bim1* double mutant strains with other datasets. Table S1 lists the features measured. Table S2 shows strains and plasmids used in this study. Table S3 shows mean values of 90 features for single mutants. Table S4 shows mean values of 90 features for double deletion with *bni1Δ*. Table S5 shows mean values of 90 features for double deletion with *bim1Δ*. Table S6 shows p-values generated for single mutants and *bni1Δ* and *bim1Δ* double mutants on three spindle specific features. Table S7 lists essential genes analyzed for spindle defect by HCS. Online supplemental material is available at <http://www.jcb.org/cgi/content/full/jcb.200909013/DC1>.

We thank Taras Makhnevych, Huiming Ding, Bilal Sheik, Grischa Chandy, Neal Glikman, and Timothy Schwartz for technical help.

F.J. Vizeacoumar, C. Boone, and B.J. Andrews conceived and designed the experiments. F.J. Vizeacoumar and N. van Dyk performed the experiments. F.J. Vizeacoumar, F.S. Vizeacoumar, V. Cheung, and J. Li analyzed the data. Y. Sydorsky generated Fig. 5 A, Z, Li, N. Case, F.S. Vizeacoumar, A. Datti, C. Nislow, B. Frey, B. Raught, Z. Zhang, and K. Bloom provided technical support/reagents/materials/analysis tools. F.J. Vizeacoumar, C. Boone, and B.J. Andrews wrote the paper.

This work was supported by a postdoctoral fellowship from the Best Foundation to F.J. Vizeacoumar and a grant from the Canadian Institutes of Health Research to B.J. Andrews and C. Boone (GSP-41567). Infrastructure for high content screening and SGA analysis in the Boone and Andrews laboratory was acquired with funds from the Canadian Foundation for Innovation and the Ontario Innovation Trust. Our SGA laboratories are supported by funds from Genome Canada through the Ontario Genomics Institute.

Submitted: 2 September 2009

Accepted: 3 December 2009

References

- Bandyopadhyay, S., R. Kelley, N.J. Krogan, and T. Ideker. 2008. Functional maps of protein complexes from quantitative genetic interaction data. *PLoS Comput. Biol.* 4:e1000065. doi:10.1371/journal.pcbi.1000065
- Bishop, C. 2006. Pattern Recognition and Machine Learning. New York, Springer. 738 pp.
- Blower, M.D., M. Nachury, R. Heald, and K. Weis. 2005. A Rae1-containing ribonucleoprotein complex is required for mitotic spindle assembly. *Cell* 121:223–234. doi:10.1016/j.cell.2005.02.016
- Boone, C., H. Bussey, and B.J. Andrews. 2007. Exploring genetic interactions and networks with yeast. *Nat. Rev. Genet.* 8:437–449. doi:10.1038/nrg2085
- Buonomo, S.B., K.P. Rabitsch, J. Fuchs, S. Gruber, M. Sullivan, F. Uhlmann, M. Petronczki, A. Tóth, and K. Nasmyth. 2003. Division of the nucleolus and its release of CDC14 during anaphase of meiosis I depends on separase, SPO12, and SLK19. *Dev. Cell.* 4:727–739. doi:10.1016/S1534-5807(03)00129-1
- Buvelot, S., S.Y. Tatsutani, D. Vermaak, and S. Biggins. 2003. The budding yeast Ipl1/Aurora protein kinase regulates mitotic spindle disassembly. *J. Cell Biol.* 160:329–339. doi:10.1083/jcb.200209018
- Byers, B., and L. Goetsch. 1975. Behavior of spindles and spindle plaques in the cell cycle and conjugation of *Saccharomyces cerevisiae*. *J. Bacteriol.* 124:511–523.
- Chaudhuri, A.R., I.A. Khan, V. Prasad, A.K. Robinson, R.F. Ludueña, and L.D. Barnes. 1999. The tumor suppressor protein Fhit. A novel interaction with tubulin. *J. Biol. Chem.* 274:24378–24382. doi:10.1074/jbc.274.34.24378
- D'Amours, D., and A. Amon. 2004. At the interface between signaling and executing anaphase—Cdc14 and the FEAR network. *Genes Dev.* 18:2581–2595. doi:10.1101/gad.1247304
- Denison, C., A.D. Rudner, S.A. Gerber, C.E. Bakalarski, D. Moazed, and S.P. Gygi. 2005. A proteomic strategy for gaining insights into protein sumoylation in yeast. *Mol. Cell. Proteomics.* 4:246–254. doi:10.1074/mcp.M400154-MCP200
- Enyenihi, A.H., and W.S. Saunders. 2003. Large-scale functional genomic analysis of sporulation and meiosis in *Saccharomyces cerevisiae*. *Genetics.* 163:47–54.
- Fesquet, D., P.J. Fitzpatrick, A.L. Johnson, K.M. Kramer, J.H. Toyn, and L.H. Johnston. 1999. A Bub2p-dependent spindle checkpoint pathway regulates the Dbf2p kinase in budding yeast. *EMBO J.* 18:2424–2434. doi:10.1093/emboj/18.9.2424
- Gassmann, R., A. Carvalho, A.J. Henzing, S. Ruchaud, D.F. Hudson, R. Honda, E.A. Nigg, D.L. Gerloff, and W.C. Earnshaw. 2004. Borealin: a novel chromosomal passenger required for stability of the bipolar mitotic spindle. *J. Cell Biol.* 166:179–191. doi:10.1083/jcb.200404001
- Geymonat, M., A. Spanos, S.J. Smith, E. Wheatley, K. Rittinger, L.H. Johnston, and S.G. Sedgwick. 2002. Control of mitotic exit in budding yeast. In vitro regulation of Tem1 GTPase by Bub2 and Bfa1. *J. Biol. Chem.* 277:28439–28445. doi:10.1074/jbc.M202540200
- Giaever, G., A.M. Chu, L. Ni, C. Connelly, L. Riles, S. Véronneau, S. Dow, A. Lucau-Danila, K. Anderson, B. André, et al. 2002. Functional profiling of the *Saccharomyces cerevisiae* genome. *Nature.* 418:387–391. doi:10.1038/nature00935
- Graumann, J., L.A. Dunipace, J.H. Seol, W.H. McDonald, J.R. Yates III, B.J. Wold, and R.J. Deshaies. 2004. Applicability of tandem affinity purification MudPIT to pathway proteomics in yeast. *Mol. Cell. Proteomics.* 3:226–237. doi:10.1074/mcp.M300099-MCP200
- Gupta, M.L. Jr., P. Carvalho, D.M. Roof, and D. Pellman. 2006. Plus end-specific depolymerase activity of Kip3, a kinesin-8 protein, explains its role in positioning the yeast mitotic spindle. *Nat. Cell Biol.* 8:913–923. doi:10.1038/ncb1457
- Hannich, J.T., A. Lewis, M.B. Kroetz, S.J. Li, H. Heide, A. Emili, and M. Hochstrasser. 2005. Defining the SUMO-modified proteome by multiple approaches in *Saccharomyces cerevisiae*. *J. Biol. Chem.* 280:4102–4110. doi:10.1074/jbc.M413209200
- Hess, H., J. Clemmens, D. Qin, J. Howard, and V. Vogel. 2001. Light-controlled molecular shuttles made from motor proteins carrying cargo on engineered surfaces. *Nano Lett.* 1:235–239. doi:10.1021/nl015521e
- Jensen, S., A.L. Johnson, L.H. Johnston, and M. Segal. 2004. Temporal coupling of spindle disassembly and cytokinesis is disrupted by deletion of LTE1 in budding yeast. *Cell Cycle.* 3:817–822.
- Jeram, S.M., T. Srikumar, P.G. Pedrioli, and B. Raught. 2009. Using mass spectrometry to identify ubiquitin and ubiquitin-like protein conjugation sites. *Proteomics.* 9:922–934. doi:10.1002/pmic.200800666

- Johnston, M. 1999. Feasting, fasting and fermenting. Glucose sensing in yeast and other cells. *Trends Genet.* 15:29–33. doi:10.1016/S0168-9525(98)01637-0
- Jones, H.D., M. Schliwa, and D.G. Drubin. 1993. Video microscopy of organelle inheritance and motility in budding yeast. *Cell Motil. Cytoskeleton.* 25:129–142. doi:10.1002/cm.970250203
- Kaufman, L., and P.J. Rousseeuw. 1990. Finding groups in data: an introduction to cluster analysis. Wiley, New York. 342 pp.
- Khmelniskii, A., and E. Schiebel. 2008. Assembling the spindle midzone in the right place at the right time. *Cell Cycle.* 7:283–286.
- Khmelniskii, A., C. Lawrence, J. Roostalu, and E. Schiebel. 2007. Cdc14-regulated midzone assembly controls anaphase B. *J. Cell Biol.* 177:981–993. doi:10.1083/jcb.200702145
- Kilmartin, J.V., and A.E. Adams. 1984. Structural rearrangements of tubulin and actin during the cell cycle of the yeast *Saccharomyces*. *J. Cell Biol.* 98:922–933. doi:10.1083/jcb.98.3.922
- Kittler, R., G. Putz, L. Pelletier, I. Poser, A.K. Heninger, D. Drechsel, S. Fischer, I. Konstantinova, B. Habermann, H. Grabner, et al. 2004. An endoribonuclease-prepared siRNA screen in human cells identifies genes essential for cell division. *Nature.* 432:1036–1040. doi:10.1038/nature03159
- Knockleby, J., and J. Vogel. 2009. The COMA complex is required for Sli15/INCENP-mediated correction of defective kinetochore attachments. *Cell Cycle.* 8:2570–2577.
- Komarnitsky, S.I., Y.C. Chiang, F.C. Luca, J. Chen, J.H. Toyn, M. Winey, L.H. Johnston, and C.L. Denis. 1998. DBF2 protein kinase binds to and acts through the cell cycle-regulated MOB1 protein. *Mol. Cell Biol.* 18:2100–2107.
- Lee, L., S.K. Klee, M. Evangelista, C. Boone, and D. Pellman. 1999. Control of mitotic spindle position by the *Saccharomyces cerevisiae* formin Bni1p. *J. Cell Biol.* 144:947–961. doi:10.1083/jcb.144.5.947
- Makhnevych, T., Y. Sydorsky, X. Xin, T. Srikumar, F.J. Vizeacoumar, S.M. Jeram, Z. Li, S. Bahr, B.J. Andrews, C. Boone, and B. Raught. 2009. Global map of SUMO function revealed by protein-protein interaction and genetic networks. *Mol. Cell.* 33:124–135. doi:10.1016/j.molcel.2008.12.025
- Marston, A.L., B.H. Lee, and A. Amon. 2003. The Cdc14 phosphatase and the FEAR network control meiotic spindle disassembly and chromosome segregation. *Dev. Cell.* 4:711–726. doi:10.1016/S1534-5807(03)00130-8
- Melchior, F. 2000. SUMO—nonclassical ubiquitin. *Annu. Rev. Cell Dev. Biol.* 16:591–626. doi:10.1146/annurev.cellbio.16.1.591
- Morishita, T., H. Mitsuzawa, M. Nakafuku, S. Nakamura, S. Hattori, and Y. Anraku. 1995. Requirement of *Saccharomyces cerevisiae* Ras for completion of mitosis. *Science.* 270:1213–1215. doi:10.1126/science.270.5239.1213
- Müller, S., C. Hoegge, G. Pyrowolakis, and S. Jentsch. 2001. SUMO, ubiquitin's mysterious cousin. *Nat. Rev. Mol. Cell Biol.* 2:202–210. doi:10.1038/35056591
- Ohya, Y., J. Sese, M. Yukawa, F. Sano, Y. Nakatani, T.L. Saito, A. Saka, T. Fukuda, S. Ishihara, S. Oka, et al. 2005. High-dimensional and large-scale phenotyping of yeast mutants. *Proc. Natl. Acad. Sci. USA.* 102:19015–19020. doi:10.1073/pnas.0509436102
- Panse, V.G., U. Hardeland, T. Werner, B. Kuster, and E. Hurt. 2004. A proteome-wide approach identifies sumoylated substrate proteins in yeast. *J. Biol. Chem.* 279:41346–41351. doi:10.1074/jbc.M407950200
- Pereira, G., and E. Schiebel. 2003. Separase regulates INCENP-Aurora B anaphase spindle function through Cdc14. *Science.* 302:2120–2124. doi:10.1126/science.1091936
- Pereira, G., T. Höfken, J. Grindlay, C. Manson, and E. Schiebel. 2000. The Bub2p spindle checkpoint links nuclear migration with mitotic exit. *Mol. Cell.* 6:1–10. doi:10.1016/S1097-2765(00)00002-2
- Pereira, G., T.U. Tanaka, K. Nasmyth, and E. Schiebel. 2001. Modes of spindle pole body inheritance and segregation of the Bfa1p-Bub2p checkpoint protein complex. *EMBO J.* 20:6359–6370. doi:10.1093/emboj/20.22.6359
- Pruyne, D., A. Legesse-Miller, L. Gao, Y. Dong, and A. Bretscher. 2004. Mechanisms of polarized growth and organelle segregation in yeast. *Annu. Rev. Cell Dev. Biol.* 20:559–591. doi:10.1146/annurev.cellbio.20.010403.103108
- Ro, H.S., S. Song, and K.S. Lee. 2002. Bfa1 can regulate Tem1 function independently of Bub2 in the mitotic exit network of *Saccharomyces cerevisiae*. *Proc. Natl. Acad. Sci. USA.* 99:5436–5441. doi:10.1073/pnas.062059999
- Robinson, M.D., J. Grigull, N. Mohammad, and T.R. Hughes. 2002. FunSpec: a web-based cluster interpreter for yeast. *BMC Bioinformatics.* 3:35. doi:10.1186/1471-2105-3-35
- Ruchaud, S., M. Carmenta, and W.C. Earnshaw. 2007. The chromosomal passenger complex: one for all and all for one. *Cell.* 131:230–231. doi:10.1016/j.cell.2007.10.002
- Rutherford, S.L., and S. Lindquist. 1998. Hsp90 as a capacitor for morphological evolution. *Nature.* 396:336–342. doi:10.1038/24550
- Seeler, J.S., and A. Dejean. 2003. Nuclear and unclear functions of SUMO. *Nat. Rev. Mol. Cell Biol.* 4:690–699. doi:10.1038/nrm1200
- Sheff, M.A., and K.S. Thorn. 2004. Optimized cassettes for fluorescent protein tagging in *Saccharomyces cerevisiae*. *Yeast.* 21:661–670. doi:10.1002/yea.1130
- Sopko, R., D. Huang, N. Preston, G. Chua, B. Papp, K. Kafadar, M. Snyder, S.G. Oliver, M. Cyert, T.R. Hughes, et al. 2006. Mapping pathways and phenotypes by systematic gene overexpression. *Mol. Cell.* 21:319–330. doi:10.1016/j.molcel.2005.12.011
- Stegmeier, F., and A. Amon. 2004. Closing mitosis: the functions of the Cdc14 phosphatase and its regulation. *Annu. Rev. Genet.* 38:203–232. doi:10.1146/annurev.genet.38.072902.093051
- Stegmeier, F., R. Visintin, and A. Amon. 2002. Separase, polo kinase, the kinetochore protein Slk19, and Spo12 function in a network that controls Cdc14 localization during early anaphase. *Cell.* 108:207–220. doi:10.1016/S0092-8674(02)00618-9
- Stoepel, J., M.A. Ottey, C. Kurischko, P. Hieter, and F.C. Luca. 2005. The mitotic exit network Mob1p-Dbf2p kinase complex localizes to the nucleus and regulates passenger protein localization. *Mol. Biol. Cell.* 16:5465–5479. doi:10.1091/mbc.E05-04-0337
- Sullivan, M., and F. Uhlmann. 2003. A non-proteolytic function of separase links the onset of anaphase to mitotic exit. *Nat. Cell Biol.* 5:249–254. doi:10.1038/ncb940
- Sullivan, M., C. Lehane, and F. Uhlmann. 2001. Orchestrating anaphase and mitotic exit: separase cleavage and localization of Slk19. *Nat. Cell Biol.* 3:771–777. doi:10.1038/ncb0901-771
- Thomas, S., and K.B. Kaplan. 2007. A Bir1p Sli15p kinetochore passenger complex regulates septin organization during anaphase. *Mol. Biol. Cell.* 18:3820–3834. doi:10.1091/mbc.E07-03-0201
- Tong, A.H., M. Evangelista, A.B. Parsons, H. Xu, G.D. Bader, N. Pagé, M. Robinson, S. Raghibizadeh, C.W. Hogue, H. Bussey, et al. 2001. Systematic genetic analysis with ordered arrays of yeast deletion mutants. *Science.* 294:2364–2368. doi:10.1126/science.1065810
- Tong, A.H., G. Lesage, G.D. Bader, H. Ding, H. Xu, X. Xin, J. Young, G.F. Berriz, R.L. Brost, M. Chang, et al. 2004. Global mapping of the yeast genetic interaction network. *Science.* 303:808–813. doi:10.1126/science.1091317
- Toyn, J.H., and L.H. Johnston. 1994. The Dbf2 and Dbf20 protein kinases of budding yeast are activated after the metaphase to anaphase cell cycle transition. *EMBO J.* 13:1103–1113.
- Vallee, R.B., J.C. Williams, D. Varma, and L.E. Barnhart. 2004. Dynein: An ancient motor protein involved in multiple modes of transport. *J. Neurobiol.* 58:189–200. doi:10.1002/neu.10314
- Visintin, C., B.N. Tomson, R. Rahal, J. Paulson, M. Cohen, J. Taunton, A. Amon, and R. Visintin. 2008. APC/C-Cdh1-mediated degradation of the Polo kinase Cdc5 promotes the return of Cdc14 into the nucleolus. *Genes Dev.* 22:79–90. doi:10.1101/gad.1601308
- Vizeacoumar, F.J., Y. Chong, C. Boone, and B.J. Andrews. 2009. A picture is worth a thousand words: genomics to phenomics in the yeast *Saccharomyces cerevisiae*. *FEBS Lett.* 583:1656–1661. doi:10.1016/j.febslet.2009.03.068
- Wágner, G., J. Kovács, P. Löw, F. Orosz, and J. Ovádi. 2001. Tubulin and microtubule are potential targets for brain hexokinase binding. *FEBS Lett.* 509:81–84. doi:10.1016/S0014-5793(01)03136-2
- Wohlschlegel, J.A., E.S. Johnson, S.I. Reed, and J.R. Yates III. 2004. Global analysis of protein sumoylation in *Saccharomyces cerevisiae*. *J. Biol. Chem.* 279:45662–45668. doi:10.1074/jbc.M409203200
- Wykoff, D.D., and E.K. O'Shea. 2005. Identification of sumoylated proteins by systematic immunoprecipitation of the budding yeast proteome. *Mol. Cell. Proteomics.* 4:73–83.
- Xu, H., C. Boone, and G.W. Brown. 2007. Genetic dissection of parallel sister-chromatid cohesion pathways. *Genetics.* 176:1417–1429. doi:10.1534/genetics.107.072876
- Yeh, E., R.V. Skibbens, J.W. Cheng, E.D. Salmon, and K. Bloom. 1995. Spindle dynamics and cell cycle regulation of dynein in the budding yeast, *Saccharomyces cerevisiae*. *J. Cell Biol.* 130:687–700. doi:10.1083/jcb.130.3.687
- Yoshida, S., R. Ichihashi, and A. Toh-e. 2003. Ras recruits mitotic exit regulator Lte1 to the bud cortex in budding yeast. *J. Cell Biol.* 161:889–897. doi:10.1083/jcb.200301128
- Zeng, X., J.A. Kahana, P.A. Silver, M.K. Morphew, J.R. McIntosh, I.T. Fitch, J. Carbon, and W.S. Saunders. 1999. Slk19p is a centromere protein that functions to stabilize mitotic spindles. *J. Cell Biol.* 146:415–425. doi:10.1083/jcb.146.2.415
- Zhao, X., and G. Blobel. 2005. A SUMO ligase is part of a nuclear multiprotein complex that affects DNA repair and chromosomal organization. *Proc. Natl. Acad. Sci. USA.* 102:4777–4782. doi:10.1073/pnas.0500537102
- Zhou, W., J.J. Ryan, and H. Zhou. 2004. Global analyses of sumoylated proteins in *Saccharomyces cerevisiae*. Induction of protein sumoylation by cellular stresses. *J. Biol. Chem.* 279:32262–32268. doi:10.1074/jbc.M404173200

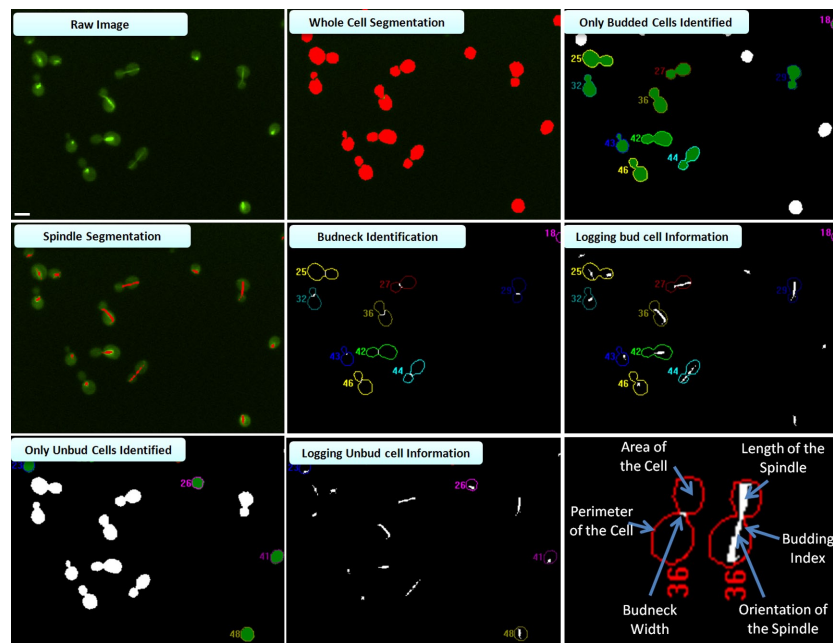
Vizeacoumar et al., <http://www.jcb.org/cgi/content/full/jcb.200909013/DC1>

Figure S1. **Steps involved in automated image analysis.** A representative image acquired from the automated imaging system and its corresponding segmented images, with major stages of image analysis are shown. Whole cell segmentation and spindle segmentation identify the objects in each image. Frames labeled as “only budded cell identified” and “only unbudded cell identified” illustrate the ability of the algorithm to classify an unseen image into these two categories. The frame labeled as “bud neck identification” shows the ability to classify cells according to their budding index. Information for budded and unbudded cells and specific regions of interest is then logged. The numbers are automatically generated by the image analysis software. Bar, 5 μ m.

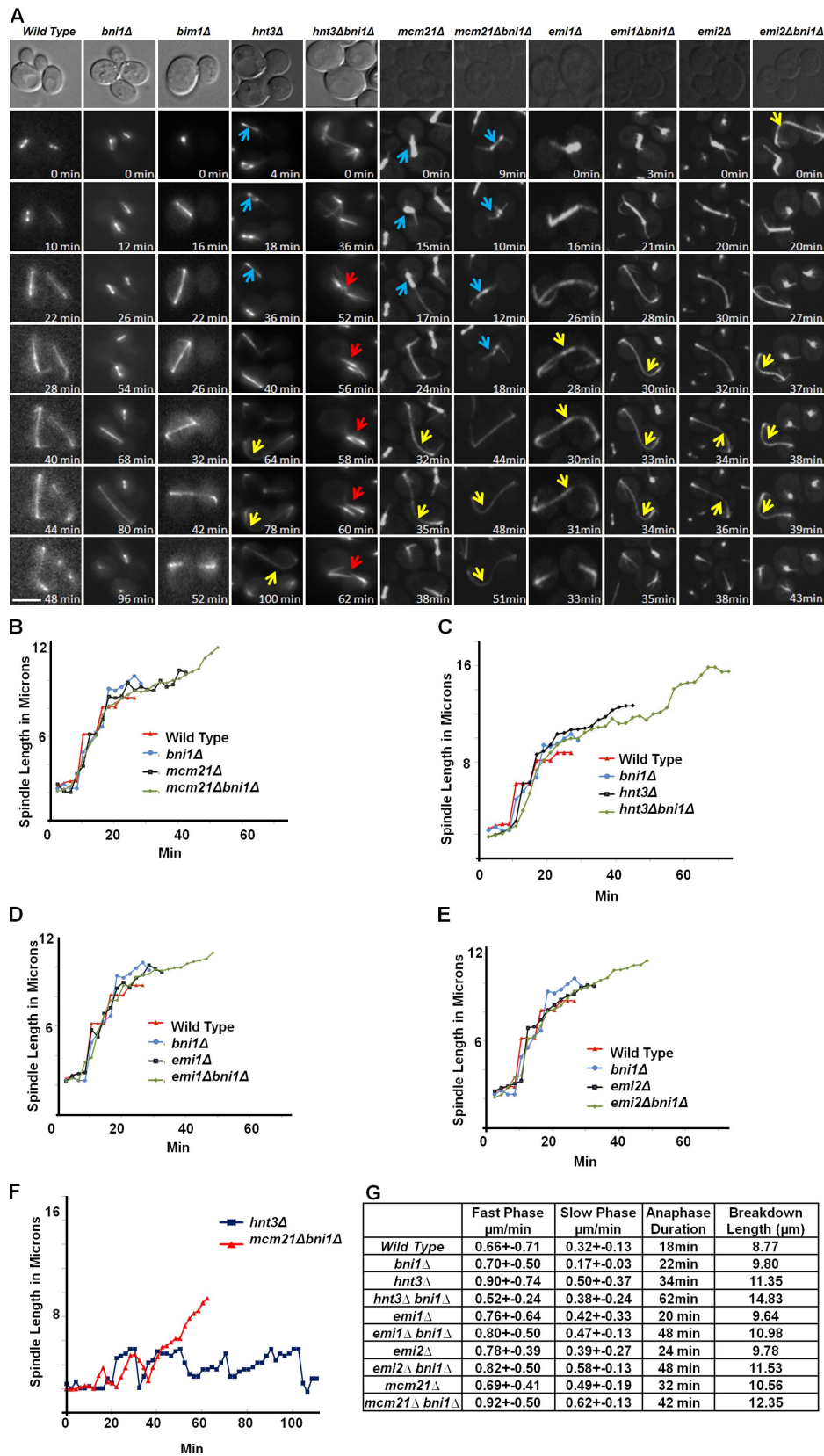


Figure S2. **Quantitation of spindle length defects in *hnt3Δ*, *mcm21Δ*, *emi1Δ*, and *emi2Δ* single and double mutant strains.** (A) Spindle disassembly phenotypes in single and double mutant cells. GFP-Tub1p-expressing cells were grown in selective medium overnight, subcultured, and imaged using a spinning disc confocal microscope (see Materials and methods). Time-lapse images of the indicated mutant cells were taken every 1 min, and representative images of cells progressing through anaphase are shown (time after initiation of image capture is shown on each micrograph). The yellow arrowheads indicate the fish hook spindle; the blue arrowheads indicate the collapsing unstable spindle; and the red arrowheads indicate swapping of the spindle poles. Bar, 5 μm.

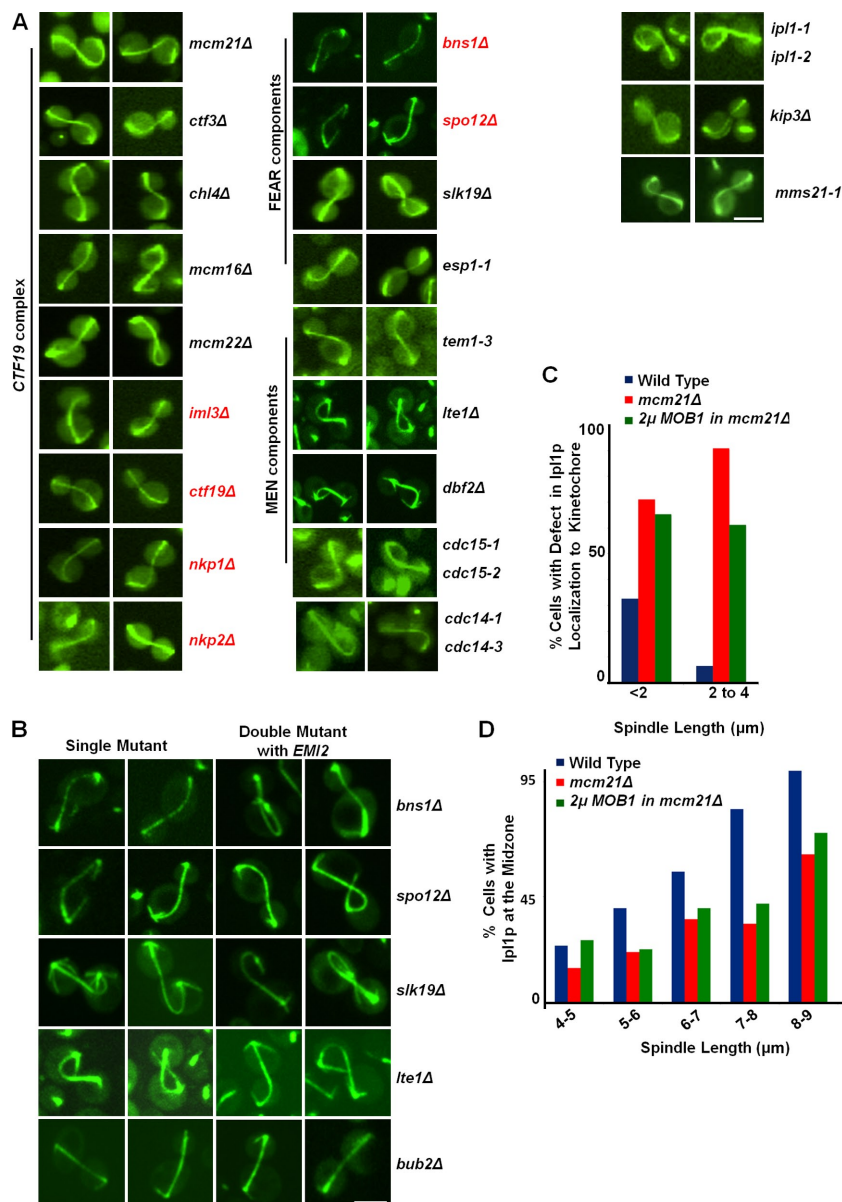


Figure S3. **Representative micrographs of fish hook spindle mutants.** (A) Fluorescence micrographs of the indicated mutant cells expressing GFP-Tub1p are shown. Components of the CTF19 or CPC complex, the MEN network, or the FEAR network are indicated. Mutants identified in our high-content screen and temperature-sensitive mutants tested directly in our study are named in black. Mutants that showed a weak fish hook spindle phenotype are highlighted in red. Temperature-sensitive mutants were grown for 3 h at the restrictive temperature before imaging. Bar, 5 μm. (B) Exacerbation of the fish hook spindle phenotype of *emi2Δ* mutant cells by deletion of FEAR/MEN components. Representative fluorescence micrographs of GFP-Tub1p are shown. Bar, 5 μm. (C and D) Quantitation of the defect in Ipl1p-GFP localization to the kinetochore during metaphase (C) and spindle midzone during anaphase (D) in wild-type, *mcm21Δ* mutant cells, and *mcm21Δ* mutant cells overexpressing *MOB1*. For kinetochore localization, cells with spindles between <2 and 2–4 μm were quantified. For midzone localization, cells with spindles 4 μm and longer were used. Cells with Ipl1p-GFP signal throughout the spindle were also considered as enriched for midzone localization in quantitation. $n > 60$ –100 cells in each spindle length category.

(B–E) Quantitation of spindle length in representative *mcm21Δ*, *hnt3Δ*, *emi1Δ*, or *emi2Δ* single mutants, or *bni1Δ* double mutant cells. The graphs show quantitation of spindle length for cells presented in Fig. S1 A or from comparable experiments. Although *mcm21Δ* and *hnt3Δ* displayed spindle instability, we calculated the fast and slow phase when these cells eventually enter anaphase and the spindle stably extends. Measurements of spindle length over time were determined using a macrosript in Metamorph for every z-stack plane in the indicated mutant images. (F) Quantitation of spindle disassembly and stability defects in representative *hnt3Δ* and *mcm21Δ* single or double mutant cells. The graphs show quantitation of spindle length for cells presented in Fig. S1 A or from comparable experiments. Measurements of spindle length over time were determined using a macrosript in Metamorph for every z-stack plane in the indicated mutant images. (G) Rates of spindle elongation in *mcm21Δ*, *hnt3Δ*, *emi1Δ*, or *emi2Δ* single mutants, or *bni1Δ* double mutant cells. Spindle elongation rates were calculated in the same time intervals used to calculate wild-type rates for the fast and slow portions of anaphase. All rates are displayed as the mean \pm standard error. The anaphase duration was calculated from when the spindle reached 2 μm in length until the when the spindle reached its full length and disassembled. Because of spindle instability in *hnt3Δ* and *mcm21Δ* mutants, anaphase duration was calculated from the time point at which no more spindle collapse was seen to the time of disassembly. The breakdown length was calculated using the final time point before spindle disassembly.

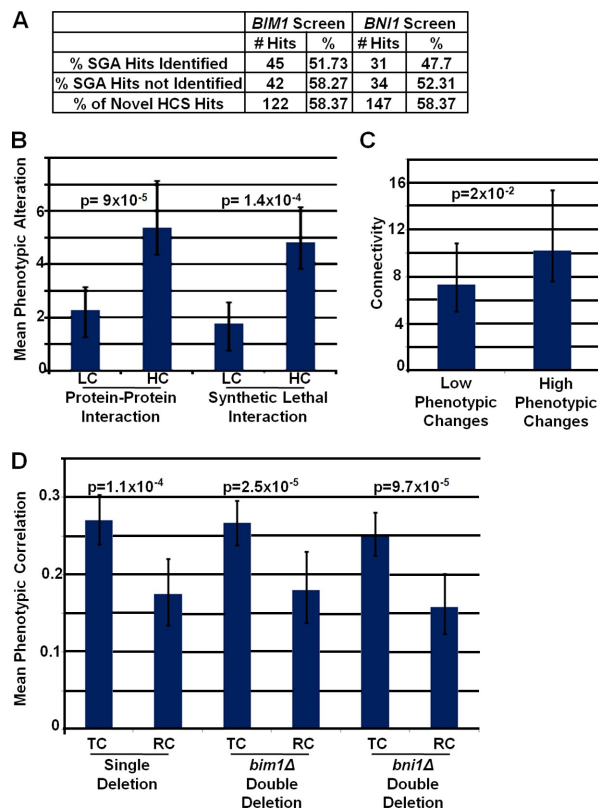


Figure S4. Correlation of the phenotypic changes in single mutant and *bni1* or *bim1* double mutant strains with other datasets. (A) Summary of genes identified in SGA screens for synthetic lethality or synthetic sick phenotypes (SGA hits) and in our high content cell biological screens (HCS hits). SGA hits in the *BIM1* screen or *BNI1* screen are those genes that showed synthetic lethality with either *bim1Δ* or *bni1Δ*, respectively. Novel HCS hits in the *BIM1* screen or *BNI1* screen are those genes that showed phenotypic abnormality with either *bim1Δ* or *bni1Δ*, respectively. (B) Highly connected members of protein and genetic interaction networks tend to have more phenotypic variation in morphological profiles. For genetic interaction tests, we compared our phenotypic profiling results to information in the BioGrid database (<http://www.thebiogrid.org/>), and protein-protein interaction information was derived from the DIP database (<http://dip.doe-mbi.ucla.edu/>). The plot shows a comparison of the number of mean phenotypic changes seen in *bim1Δ* double mutants relative to wild-type for the least connected and most highly connected proteins/genes in protein interaction and synthetic lethal networks. P-values were derived using a Mann-Whitney *U* test (see Materials and methods). The mean phenotypic change for the selected genes and the 95% confidence interval of the mean are shown. The confidence interval was derived from 5,000 bootstrap resamplings. LC, least connected genes; HC, highly connected genes. (C) Genes with increased mean phenotypic changes are highly connected for synthetic lethal network interactions. The plot shows a comparison of connectivity in the synthetic lethal network in *bim1Δ* strains between genes whose deletion causes the lowest phenotypic changes and those that cause the highest phenotypic changes. Connectivity is defined as the number of synthetic lethal interactions of a given gene. The mean phenotypic change for the selected genes and the 95% confidence interval of the mean are shown. The confidence interval was derived from 5,000 bootstrap resamplings (see Materials and methods). (D) Genes encoding components of the same protein complexes (within complex) have high mean phenotypic correlation. Single mutants and *bni1Δ* or *bim1Δ* double mutants defective in genes encoding proteins in the same protein complex were analyzed for phenotypic similarity. A total of ~274 literature-curated protein complexes and a similar set of randomly generated protein complexes were examined for the correlation of their morphological profile (see Materials and methods). The plot shows a comparison of the mean phenotypic correlation seen in the single and double mutants of *bni1Δ* and *bim1Δ*. A statistically significant mean phenotypic correlation within complexes as opposed to the randomly chosen set and their respective p-values are shown. RC, random complex; TC, true complex.

Table S1. List of features measured and feature index used for high-content screen data mining

Parameter	Unbudded				Small bud				Medium bud				Large bud			
					Small bud		Small bud-specific		Medium bud		Medium bud-specific		Large bud		Large bud-specific	
		Mother	Daughter		Mother	Daughter	Mother	Daughter	Mother	Daughter	Mother	Daughter	Mother	Daughter	Mother	Daughter
Mean area	4	4	4	4										4	4	
Mean perimeter	4	4	4	4										4	4	
Mean length	4	4	4	4										4	4	
Mean breadth	4	4	4	4										4	4	
Mean shape factor	4	4	4	4										4	4	
Mean elliptical form factor	4	4	4	4										4	4	
Mean equivalent prolate volume	4	4	4	4										4	4	
Mean equivalent oblate volume	4	4	4	4										4	4	
Cell count	1															1
Mean bud neck width																4
Metaphase spindle count																1
Anaphase spindle count																1
Metaphase spindle mean fiber length																4
Metaphase spindle mean spindle distribution to bud neck																4
Metaphase spindle mean spindle orientation																4
Anaphase spindle mean fiber length																4
Anaphase spindle mean spindle distribution to bud neck																4
Anaphase spindle mean spindle orientation																4
Percentage with anaphase spindle																1
Percentage with metaphase spindle																1
Percentage of cells	1															1
Percentage unbudded with one SPB	1															1
Percentage of unbudded with two SPB	1															1
Percentage with more than two SPB	1															1

Note: Each feature measured has four parameters, namely: mean, coefficient of variance, minimum value and a maximum value. Blank cells indicate that the criteria is not applicable.

Table S2. Strains and plasmids used in this study

Strain	Genotype	Source
Y8835	<i>MATa ura3Δ::natR can1Δ::STE2pr-Sp_HIS5 lyp1Δ; his3Δ1 leu2Δ0ura3Δ0 met15Δ0 LYS2+</i>	Boone laboratory
Y9273	<i>MATa bni1Δ::NatR can1Δ::STE2pr-Sp_HIS5 lyp1Δ ura3Δ0 leu2Δ0 his3Δ1 met15Δ0 LYS2Δ0</i>	Boone laboratory
Y8394	<i>MATa bim1Δ::NatR can1Δ::STE2pr-Sp_HIS5 lyp1Δ::STE3pr-LEU2 ura3Δ0 leu2Δ0 his3Δ1 met15Δ0</i>	Boone laboratory
Y12476	<i>MATa hnt3Δ::KanMX4 bni1Δ::NatR ura3Δ0 leu2Δ0 his3Δ1 met15Δ0 LYS2+</i>	This study
Y12477	<i>MATa mcm21Δ::KanMX4 bni1Δ::NatR ura3Δ0 leu2Δ0 his3Δ1 met15Δ0 LYS2+</i>	This study
Y12478	<i>MATa emi1Δ::KanMX4 bni1Δ::NatR ura3Δ0 leu2Δ0 his3Δ1 met15Δ0 LYS2+</i>	This study
Y12479	<i>MATa emi2Δ::KanMX4 bni1Δ::NatR ura3Δ0 leu2Δ0 his3Δ1 met15Δ0 LYS2+</i>	This study
Y12488	<i>MATa slk19Δ::KanMX4 mcm21Δ::NatR ura3Δ0 leu2Δ0 his3Δ1 met15Δ0 LYS2+</i>	This study
Y12489	<i>MATa fob1Δ::KanMX4 mcm21Δ::NatR ura3Δ0 leu2Δ0 his3Δ1 met15Δ0 LYS2+</i>	This study
Y12604	<i>MATa dbf2Δ::KanMX4 emi2Δ::NatR ura3Δ0 leu2Δ0 his3Δ1 met15Δ0 LYS2+</i>	This study
Y12605	<i>MATa lte1Δ::KanMX4 emi2Δ::NatR ura3Δ0 leu2Δ0 his3Δ1 met15Δ0 LYS2+</i>	This study
Y12606	<i>MATa bns1Δ::KanMX4 emi2Δ::NatR ura3Δ0 leu2Δ0 his3Δ1 met15Δ0 LYS2+</i>	This study
Y12607	<i>MATa spo12Δ::KanMX4 emi2Δ::NatR ura3Δ0 leu2Δ0 his3Δ1 met15Δ0 LYS2+</i>	This study
Y12608	<i>MATa slk19Δ::KanMX4 emi2Δ::NatR ura3Δ0 leu2Δ0 his3Δ1 met15Δ0 LYS2+</i>	This study
Y12609	<i>MATa bub2Δ::KanMX4 emi2Δ::NatR ura3Δ0 leu2Δ0 his3Δ1 met15Δ0 LYS2+</i>	This study
Y12485	<i>MATa mcm21Δ::NatR SLI15-GFP::HIS3 ura3Δ0 leu2Δ0 his3Δ1 lys2Δ0 MET15+</i>	This study
Y12486	<i>MATa mcm21Δ::NatR IPL1-GFP::HIS3 ura3Δ0 leu2Δ0 his3Δ1 lys2Δ0 MET15+</i>	This study
Y12487	<i>MATa mcm21Δ::NatR BIR1-GFP::HIS3 ura3Δ0 leu2Δ0 his3Δ1 lys2Δ0 MET15+</i>	This study
Y12616	<i>MATa mcm21Δ::NatR CDC14-GFP::HIS3 ura3Δ0 leu2Δ0 his3Δ1 lys2Δ0 MET15+</i>	This study
Y12617	<i>MATa emi2Δ::NatR CDC14-GFP::HIS3 ura3Δ0 leu2Δ0 his3Δ1 lys2Δ0 MET15+</i>	This study
Y12618	<i>MATa dbf2Δ::NatR CDC14-GFP::HIS3 ura3Δ0 leu2Δ0 his3Δ1 lys2Δ0 MET15+</i>	This study
Y12619	<i>MATa MCM21-32R-GFP::MCM21-GFP ura3Δ0 leu2Δ0 his3Δ1 lys2Δ0 MET15+</i>	This study
Y12610	<i>MATa ubc9-2::NatR MCM21-TAP::HIS3 leu2Δ0 ura3Δ0</i>	This study
Y12611	<i>MATa ubc9-2::NatR AME1-TAP::HIS3 leu2Δ0 ura3Δ1</i>	This study
Y12612	<i>MATa ubc9-2::NatR OKP1-TAP::HIS3 leu2Δ0 ura3Δ2</i>	This study
Y12613	<i>MATa ubc9-2::NatR CTF19-TAP::HIS3 leu2Δ0 ura3Δ3</i>	This study
Y12614	<i>MATa ubc9-2::NatR IPL1-GFP::HIS3 leu2Δ0 ura3Δ3</i>	This study
Y12615	<i>MATa ubc9-2::NatR SLI15-GFP::HIS3 leu2Δ0 ura3Δ3</i>	This study
Y07353	<i>MATa cdc14-1::KanMX4 his3Δ1, leu2Δ0, ura3Δ0, met15Δ0</i>	Boone laboratory
Y07385	<i>MATa cdc14-3::KanMX4 his3Δ1, leu2Δ0, ura3Δ0, met15Δ0</i>	Boone laboratory
Y11434	<i>MATa cdc15-1::KanMX4 his3Δ1, leu2Δ0, ura3Δ0, met15Δ0</i>	Boone laboratory
Y04869	<i>MATa cdc15-2::KanMX4 his3Δ1, leu2Δ0, ura3Δ0, met15Δ0</i>	Boone laboratory
Y11708	<i>MATa esp1-1::KanMX4 his3Δ1, leu2Δ0, ura3Δ0, met15Δ0</i>	Boone laboratory
Y07424	<i>MATa ipl1-1::KanMX4 his3Δ1, leu2Δ0, ura3Δ0, met15Δ0</i>	Boone laboratory
Y07820	<i>MATa ipl1-2::KanMX4 his3Δ1, leu2Δ0, ura3Δ0, met15Δ0</i>	Boone laboratory
Y07908	<i>MATa tem1-3::KanMX4 his3Δ1, leu2Δ0, ura3Δ0, met15Δ0</i>	Boone laboratory
P5575	<i>pGFP-Tub1 URA3 CEN</i>	This study
P5576	<i>pMob1 LEU2 2μ</i>	Boone laboratory
P5582	<i>pRFP-Tub1 URA3 CEN</i> (the term RFP represents mCherry version of the red fluorescent protein)	This study
P5583	<i>pMcm21-32R-TAP LEU2 CEN</i>	This study

The single deletion strains used individually or for the entire genome analysis were obtained from the Yeast Deletion Library.

Table S3 lists mean values of 90 features for single mutants. Table S4 lists mean values of 90 features for double deletion with *bni1Δ*. Table S5 lists mean values of 90 features for double deletion with *bim1Δ*. Table S6 lists p-values generated for single and *bni1Δ* and *bim1Δ* double mutants on three spindle-specific features. Table S7 list of essential genes analyzed for spindle defect by HCS.